

# Continuously unique anisotropic Critical State hyperplasticity

William Michael Coombs

School of Engineering & Computing Sciences, Durham University,  
Science Site, South Road, Durham, DH1 3LE, UK.  
e-mail: w.m.coombs@durham.ac.uk

July 28, 2016

## Abstract

This paper presents the theoretical development and methodological motivation of a single surface anisotropic hyperplasticity model. The model extends the isotropic family of models developed by Coombs and Crouch [19] by: (i) introducing anisotropic shearing into the yield surface, (ii) relating two of the material constants to a single physical quantity and (iii) using a more physically realistic pressure sensitive elastic free energy function. This model overcomes the difficulty of determining the constants of the isotropic two-parameter surface by analytically relating them to a single experimentally measurable physical quantity, namely the normalised hydrostatic position of the Critical State. This provides a model with a Critical State surface that is constant throughout the loading process, invariant of the level of anisotropy inherent in the yield envelope. The model is compared with experimental data from triaxial tests on Lower Cromer Till [35], contrasted against the SANIclay model of Dafalias et al. [26] and the recent model of Yang et al. [71] as well as being compared with rarely considered experimental data from hollow cylinder tests on London Clay [52].

**keywords:** anisotropy; plasticity; numerical modelling

## 1 Introduction

A large number of constitutive models have been proposed previously in the literature that are intended to capture the anisotropic behaviour of fine grain particulate media (such as clays). The majority of these models have their roots within the classical framework of Critical State Soil Mechanics (CSSM) developed in Cambridge in the 1950s and 60s by Roscoe and co-workers [58–60], and, independently, Parry [54], founded on the earlier work of Casagrande [7].

Within this theory, the modified Cam-clay (MCC) constitutive model (following on from the original Cam-clay model of Schofield and Wroth [60]) was the first hardening plasticity model to become generally accepted for the analysis of soils [68]. This formulation, with associated plastic flow and ellipsoidal yield surface is able to conceptually capture several aspects of real soil behaviour [36]. These features include a volumetric response dependent on the stress history of the material, a unique state boundary surface, for which soils states outside are inadmissible, and a unique void ratio versus Critical State stress line [36]. Despite these attractions, Yu [72] (amongst many others) commented that the MCC constitutive formulations significantly overestimate the peak stress on the *dry* side of the Critical State line (the heavily overconsolidated region) and, due to their associated flow rule, are unable to capture post-peak softening towards the Critical State in normally consolidated clays.

However, many of the modifications to the original CSSM conceptual framework were motivated, not by deep insights into the underlying physics, but rather through a wish to improve curve-fits to

specific sets of experimental data. These models have, in many cases, detracted from the elegance of the original framework. They have also tended to make the models less accessible for practising engineers.

The model presented in this paper is cast within the framework of hyperplasticity. These formulations, arising from the pioneering works of Ziegler [73] and Houlsby [41], allow the constitutive equations to be derived from a free-energy function and a dissipation rate function [44]. Once these functions have been specified, the stress-elastic strain law, yield function and flow rule can all be obtained without the requirement for any additional assumptions. For example, it is not necessary to specify a yield function and then postulate a separate plastic flow potential to define the development of inelastic straining. Textbook accounts of the thermomechanics of materials can be found in volumes by Ziegler [73] and Maugin [51], amongst others.

Several hyperplastic models have been constructed for geomaterials [9–17, 43, 44, 56, 57]. These offer fundamental improvements over the conventional plasticity formulations which, in a number of cases, fail to satisfy fundamental thermodynamic principles.

Valid motivations for extending the original models developed within CSSM stem from the fact the original isotropic models are unable to capture the variation of stiffness and strength with variations in material fabric. Over the last 30 years a number of models have been proposed to account for this directional bias, including [3, 24, 25, 27, 33, 47, 48, 55, 62, 65, 66], amongst many others. These models include some inelastic shearing, or rotation, of the yield surface off the hydrostatic axis to account for the strength directional dependence. The majority of these extensions fail to maintain a unique Critical State surface invariant to the level of anisotropy with the material fabric and include a dependence on the Lode angle. This shortcoming was addressed by the work of Wheeler *et al.* [65], in triaxial stress space, and later by Coombs *et al.* [24] in generalised 6-component stress space, however their formulations only maintained an asymptotically unique Critical State surface. That is, the instantaneous position of the Critical State surface during the loading process depended on the degree of shearing of the yield envelope. Here that dependency is removed through linking two yield surface shape parameters, proposed by Collins and Hilder [12] that control the level of dissipation under deviatoric plastic deformation, to the position of the Critical State.

The layout of the paper is as follows. Section 2 presents the theoretical development of the anisotropic single surface model including: (i) elasticity relationship, (ii) dissipation, (iii) Lode angle dependency (LAD), (iv) parameters controlling the shape of the yield surface, (v) isotropic expansion or contraction and (vi) development of anisotropic shearing. Section 3 presents the model’s calibration procedure and compares the proposed model with experimental data on Lower Cromer Till [35] and with the SANIclay model of Dafalias *et al.* [26] and the recent model of Yang *et al.* [71]. This section also presents a comparison of hollow cylinder experimental data on London Clay with the proposed model. Brief conclusions are drawn in Section 4.

## 2 Anisotropic constitutive formulation

This section presents the theoretical development of the single surface anisotropic model.

The elegance of hyperplasticity theory stems from its ability to derive a complete constitutive model from two scalar potentials: a free-energy function,  $\Psi$ , and a dissipation function,  $\dot{\Phi}$  [44]. In this paper the free-energy function is split into two components

$$\Psi = \Psi_1 + \Psi_2, \quad (1)$$

where  $\Psi_1$  is the elastic free-energy and  $\Psi_2$  is the plastic free-energy. Sections 2.1 and 2.2 describe the elastic free-energy and dissipation functions, respectively, which are used to develop the stress versus elastic strain relationship, the yield function and the direction of inelastic straining. Section 2.3 discusses the implementation of a LAD in the model and Section 2.4 derives a relationship for the

yield surface shape parameters based on the level of induced anisotropy. The model's hardening laws are derived from  $\Psi_2$  in Section 2.5.

## 2.1 Elastic free-energy function

The model proposed in this paper uses an elastic free energy function with pressure sensitive bulk and shear moduli [42]

$$\Psi_1 = \kappa p_r \exp(\Omega) + G \gamma_{ij}^e \gamma_{ij}^e, \quad (2)$$

where  $\Omega = (\varepsilon_v^e - \varepsilon_{v0}^e)/\kappa$  and  $G = G_0 + \alpha^e p_r \exp(\Omega)$ . The elastic strain measures are given by  $\varepsilon_v^e = \varepsilon_{ii}^e$  and  $\gamma_{ij}^e = \varepsilon_{ij}^e - \varepsilon_v^e \delta_{ij}/3$ , where  $\delta_{ij}$  is the Kronecker delta tensor.  $\kappa$  is the bi-logarithmic elastic compressibility index (the gradient of the drained unloading line in the bi-logarithmic void ratio versus hydrostatic pressure plane),  $G_0$  is the constant component of the shear modulus,  $p_r$  is the reference pressure,  $\varepsilon_{v0}^e$  is the elastic volumetric strain at that reference pressure and  $\alpha^e$  is a dimensionless variable that controls the coupling between the moduli. Setting  $\alpha^e = 0$ , we recover a relationship with a pressure sensitive bulk but constant shear moduli. Taking the partial derivative of (2) with respect to the elastic strain, the Cauchy stress is given by

$$\sigma_{ij} = p \delta_{ij} + 2G \gamma_{ij}^e \quad \text{where} \quad p = p_r \exp(\Omega) \left( 1 + \frac{\alpha^e}{\kappa} (\gamma_{ij}^e \gamma_{ij}^e) \right) \quad (3)$$

Taking the second derivative of the free energy function with respect to elastic strain, provides the non-linear elastic stiffness matrix

$$D_{ijkl}^e = \left( \frac{p}{\kappa} - \frac{2G}{3} \right) \delta_{ij} \delta_{kl} + 2G (I_{ijkl}) + \frac{2p_r \alpha^e}{\kappa} \exp(\Omega) (\delta_{ij} \gamma_{kl}^e + \gamma_{ij}^e \delta_{kl}), \quad (4)$$

where  $I_{ijkl}$  is a fourth order identity tensor. This form of elasticity includes stress-induced anisotropy, that is the material elastic stiffness is dependent on the level of elastic deviatoric straining. (2), as compared to laws that only include a pressure sensitive bulk modulus, is able to reproduce the anisotropic elastic unloading behaviour of soils subjected to one-dimensional ( $K_0$ ) consolidation. This was demonstrated by Borja *et al.* [5] using experimental data from tests on Vallericca clay (a stiff overconsolidated Plio-Pleistocene clay). The experimentally observed unloading response is typically characterised by an initially stiff shear modulus response that softens with reducing hydrostatic pressure. Setting  $\alpha^e = 0$ , it is only possible to provide a match to the initial unloading response at one level of hydrostatic pressure. Note that the form of stress-induced anisotropy proposed here is different that that proposed by Gajo and Bigoni [32] that contained explicit dependence on the level of inelastic straining.

## 2.2 Dissipation

The elastic free energy function, (2), provides the elastic behaviour of the model. In hyperplasticity, the other scalar-valued function required for constitutive model development is a dissipation function controlling the yield surface and direction of plastic flow.

Starting from the following dissipation function, as proposed by Collins and Hilder [12] and used by Coombs *et al.* [24],

$$\dot{\Phi} = \sqrt{(\dot{\varepsilon}_v^p + \beta_{ij} \dot{\gamma}_{ij}^p)^2 A^2 + (\dot{\varepsilon}_\gamma^p B)^2}, \quad (5)$$

where  $\dot{\varepsilon}_v^p = \dot{\varepsilon}_{ii}^p$ ,  $\dot{\varepsilon}_\gamma^p = \sqrt{\dot{\gamma}_{ij}^p \dot{\gamma}_{ij}^p}$  and  $\dot{\gamma}_{ij}^p = \dot{\varepsilon}_{ij}^p - \dot{\varepsilon}_v^p \delta_{ij}/3$ . The stress like quantities are given by  $A = (1 - \gamma)p + \gamma p_c/2$  and  $B = \bar{\rho}(\theta)M((1 - \alpha)p + \alpha \gamma p_c/2)$ , where  $p = \sigma_{ii}/3$ ,  $q = \sqrt{s_{ij}s_{ij}}$  and  $s_{ij} = \sigma_{ij} - p \delta_{ij}$ .  $\beta_{ij}$  links the volumetric and deviatoric dissipation components,  $p_c$  and  $M$  control the size and the axis-ratio of the yield surface,  $\alpha$  and  $\gamma$  control the shape of the yield surface in the

$p$ - $q$  plane and  $\bar{\rho}(\theta)$  controls the deviatoric section. Note that  $p_c$  and  $\beta_{ij}$  are deduced from the inelastic component of the free-energy function,  $\Psi_2$ , and their derivation is detailed in Section 2.5. Although, (5) was first introduced (in triaxial  $p$ - $q$  stress space) by Collins and Hilder [12] as an extension to their isotropic family of Critical State models, it was only presented conceptually, and limited to the axi-symmetric triaxial case. Following the standard procedure of manipulating the dissipation function (5), as given by [18, 21] (see Appendix A for the full derivation), it is possible to arrive at a the dimensionless anisotropic yield surface in true stress space as

$$f = \gamma(2 - \gamma)(\bar{p} - 1)\bar{B}^2 + r_{ij}^\beta r_{ij}^\beta \bar{p} \bar{A}^2 = 0, \quad (6)$$

where  $r_{ij}^\beta = r_{ij} - \beta_{ij}$ ,  $r_{ij} = s_{ij}/p$ ,  $\bar{p} = p/p_c$ ,  $\bar{A} = (1 - \gamma)\bar{p} + \gamma/2$  and  $\bar{B} = \bar{\rho}(\theta)M((1 - \alpha)\bar{p} + \alpha\gamma/2)$ . The direction of plastic flow similarly follows from the dissipation function as

$$(g, \sigma)_{ij} = 2/3(\bar{B}^2(\bar{p} - \gamma/2) - \bar{A}^2 \bar{p}(r_{kl}^\beta \beta_{kl}))\delta_{ij} + 2\bar{A}^2 \bar{p} r_{ij}^\beta, \quad (7)$$

where the derivation is given in Appendix A. It should be apparent from the second term in (6) that introducing a cross-coupling in the rate of dissipation function results in the yield surface being sheared off the hydrostatic axis, where  $\beta_{ij}$  is a second order, traceless (deviatoric), tensor measure of this shearing. If  $\beta_{ij} = 0$  we recover an isotropic modified Cam clay (MCC) yield surface, with the ellipsoid's major axis coincident with the hydrostatic axis.

### 2.3 Lode angle dependency

Including  $\bar{\rho}(\theta)$  in  $\bar{B}$  introduces a Lode angle dependency (LAD) into the yield envelope, where  $\bar{\rho}(\theta)$  is the normalised deviatoric yield radius and  $\theta$  the Lode angle. In this paper, the model is presented with a Willam and Warnke (W-W) [67] LAD that can be expressed as [66]

$$\bar{\rho}(\theta) = \frac{a_1 C + \sqrt{2a_1 C^2 + a_2}}{2a_1 C^2 + 1} \in [\bar{\rho}_e, 1] \quad (8)$$

where  $a_1 = 2(1 - \bar{\rho}_e^2)/(2\bar{\rho}_e - 1)^2$ ,  $a_2 = (5\bar{\rho}_e^2 - 4\bar{\rho}_e)/(2\bar{\rho}_e - 1)^2$ ,  $C = \cos(\pi/6 - \theta)$  and  $\bar{\rho}_e \in [0.5, 1]$  is the normalised deviatoric yield radius under triaxial extension to that under compression. To preserve convexity of the yield surface, the W-W LAD is based on a local measure of the Lode angle,  $\theta$ , from the major,  $\beta_{ij}$ , axis of the surface. This is achieved by measuring the second and third deviatoric stress invariants ( $J_2$  and  $J_3$ ) based on the deviatoric distance from the axis of anisotropy rather than the standard deviatoric measure  $s_{ij}$ . This local Lode angle is given by

$$\theta = \frac{1}{3} \arcsin \left( \frac{-3\sqrt{3}}{2} \frac{J_3}{J_2^{3/2}} \right) \in [-\pi/6, \pi/6], \quad (9)$$

where  $J_2 = \frac{1}{2}(r_{ij}^\beta r_{ji}^\beta)$  and  $J_3 = \frac{1}{3}(r_{ij}^\beta r_{jk}^\beta r_{ki}^\beta)$ . As mentioned in the previous section,  $\beta_{ij}$  corresponds to a shearing of the yield surface in the deviatoric direction, rather than a rotation away from the hydrostatic axis. This allows the inclusion of a LAD with the knowledge that an initially convex yield surface will remain convex for any degree of shearing. It is also worth noting that the W-W LAD is convex for  $\bar{\rho}_e \in [0.5, 1]$  whereas several other LAD become concave depending on the choice of  $\bar{\rho}_e$  (or rather the friction angle).

An alternative procedure for a non-circular deviatoric section is to introduce additional stress invariants into the yield equation (for example, see the works of [49] and [50]). However, the use of a LAD allows several deviatoric profiles to be included within the same framework by simply changing the form of  $\bar{\rho}(\theta)$ , the same cannot be said when using stress invariants. Several other LADs are available in the literature, for example see the work of [1, 2, 4, 23, 29, 38, 49, 50]. See the work of Bardet [2] for a comprehensive review of these LAD and that of Coombs [18] for a more detailed comparison of with experimental data.

## 2.4 Yield surface shape parameters

The dissipation function contains two parameters that control the shape of the yield surface in  $p$ - $q$  stress space, namely  $\alpha$  and  $\gamma$  (in addition to  $M$ ,  $\bar{\rho}^e$  and  $p_c$ ). These shape parameters can be used to adapt the yield surface and direction of plastic flow to the behaviour of different particulate media. However, they also introduce two additional constants that must be calibrated.

Introducing anisotropy into the dissipation function results in the loss of uniqueness of the Critical State locus (position of isochoric flow). Although this does not imply that the Critical State surface is no longer unique, it does remove some of the elegance of the isotropic two-parameter Critical State model proposed by Collins and co-workers [12, 14] and later developed further and implemented for finite-element analysis by Coombs and Crouch [19]. Note that in this work, *uniqueness* of the Critical State refers to the condition that the locus of isochoric plastic flow remains constant throughout the loading process and not just that the final Critical State position is invariant to the loading path. To recover a constant Critical State we require:

- (i) the ratio of hydrostatic pressure to the size of the yield surface where  $\dot{\varepsilon}_v^p = 0$  is constant for any level of anisotropy, that is  $\bar{p}_{cs} = (p/p_c)_{cs}$  is constant (where the subscript  $(\cdot)_{cs}$  denotes a quantity at the Critical State); and
- (ii) the stress ratio where  $\dot{\varepsilon}_v^p = 0$  is constant for any level of anisotropy, that is  $(q/p)_{cs} = M\bar{\rho}(\theta)$ .

To achieve this, first we equate the volumetric component of the direction plastic flow (7) to zero, giving

$$\bar{B}^2 = \frac{\bar{A}^2 \bar{p}(\eta - \beta)\beta}{\bar{p} - \gamma/2}, \quad (10)$$

where  $\beta = \sqrt{\beta_{ij}\beta_{ij}}$  and  $\eta = q/p$ . Note that here for simplicity (but without loss of generality of the final result) the equations are presented in conventional hydrostatic pressure,  $p$ , versus deviatoric stress,  $q$ , space. The yield function (6), provides an alternative expression for  $\bar{B}^2$

$$\bar{B}^2 = \frac{\bar{A}^2 \bar{p}(\eta - \beta)^2}{\gamma(2 - \gamma)(1 - \bar{p})}. \quad (11)$$

Combining (10) and (11) eliminates  $\alpha$  and provides an equation linking  $\gamma$  with the stress ratio at the Critical State,  $\eta_{cs}$ , and the current level of anisotropy in terms of a normalised parameter,  $\bar{\beta}$ ,

$$\gamma^2 \left( \bar{\beta}(\bar{p}_{cs} - 1) \right) + \gamma \left( (1 - \bar{\beta})/2 + 2\bar{\beta}(1 - \bar{p}_{cs}) \right) - \bar{p}_{cs}(1 - \bar{\beta}) = 0. \quad (12)$$

$\bar{\beta} = \beta/M\bar{\rho}(\theta)$  is the ratio of the gradients of the current level of anisotropy and the projected position of the Critical State. For a given level of anisotropy,  $\gamma \in [0, 1]$  can be obtained by solving the quadratic (12) and selecting the *positive root* (that is, the root associated with the + from  $\pm$  in the standard quadratic solution formula). The variation of  $\gamma$  with normalised anisotropy,  $\bar{\beta}$ , for  $\bar{p}_{cs} \in [0.2, 0.5]$  is shown in Figure 1 (i). It can be seen that reducing  $\bar{p}_{cs}$  reduces  $\gamma$ , as does increasing the level of anisotropy. In the limiting case of isotropy;  $\bar{\beta} = 0$  and  $\gamma = 2\bar{p}_{cs}$ , consistent with the isotropic formulation of Coombs and Crouch [19].

Rearranging (10) allows the second shape parameter,  $\alpha$ , to be expressed in terms of  $\bar{\beta}$  and the normalised pressure at the Critical State,  $\bar{p}_{cs}$ , as

$$\alpha = \frac{\bar{A}_{cs} \sqrt{A_\beta} - \bar{p}_{cs}}{\gamma/2 - \bar{p}_{cs}}, \quad (13)$$

where  $A_\beta = \bar{p}_{cs} \bar{\beta} (1 - \bar{\beta}) / (\bar{p}_{cs} - \gamma/2)$  and  $\bar{A}_{cs} = (1 - \gamma)\bar{p}_{cs} + \gamma/2$ . The variation of  $\alpha$  with normalised anisotropy for  $\bar{p}_{cs} \in [0.2, 0.5]$  is shown in Figure 1 (ii). Increasing the level of anisotropy initially

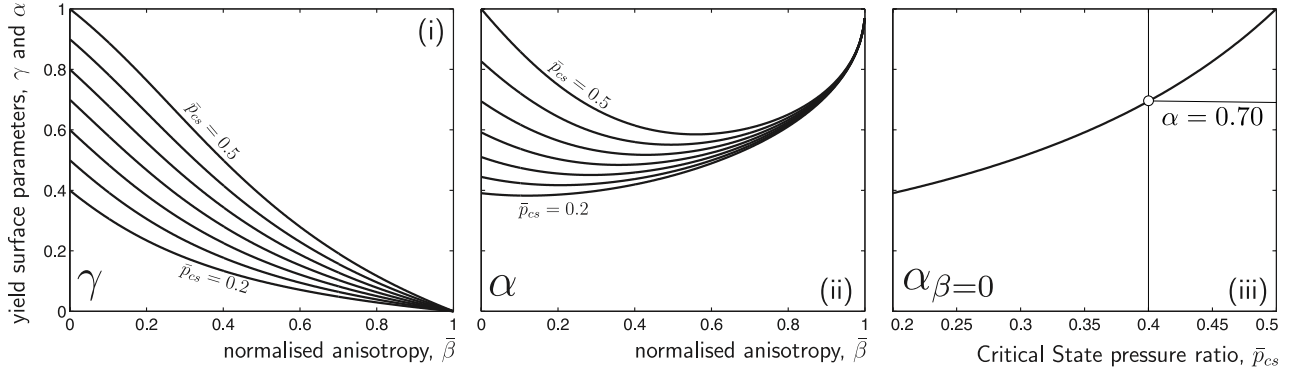


Figure 1: Yield surface parameter variation with anisotropy for  $\bar{p}_{cs} \in [0.2, 0.5]$  and  $M = 1$ : (i)  $\gamma$  versus  $\bar{\beta}$ , (ii)  $\alpha$  versus  $\bar{\beta}$  and (iii)  $\alpha$  versus  $\bar{p}_{cs}$  when  $\beta = 0$ .

causes a reduction in  $\alpha$ . However, beyond a level of anisotropy  $\alpha$  increases and the values for  $\bar{p}_{cs} \in [0.2, 0.5]$  converge as  $\bar{\beta} \rightarrow 1$ .

$\alpha$  is not well defined in the limit of  $\beta \rightarrow 0$  because when  $\beta = 0$  a unique Critical State surface is obtained for any  $\alpha \in [0, 1]$ . The value of  $\alpha$  when  $\beta \leq \text{tol}$  can be approximated by the value obtained when  $\beta = \text{tol}$ , where a tolerance (tol) of  $1 \times 10^{-5}$  provides a stable result. The variation of  $\alpha$  with  $\bar{p}_{cs} \in [0.2, 0.5]$  when  $\beta \leq \text{tol}$  is shown in Figure 1 (iii). For example, if  $\bar{p}_{cs} = 0.4$  the shape parameter,  $\alpha(\bar{\beta} = 0)$ , should be set to 0.70, as shown in the figure. Note that if  $\bar{p}_{cs} = 0.5$  and  $\beta = 0$ , we recover the classical MCC ellipsoidal yield envelope, albeit with a non-circular deviatoric section due to the imposed LAD.

One of the main motivations for introducing a Critical State that is unique throughout the loading process is that it allows two non-physical material constants,  $\alpha$  and  $\gamma$ , to be replaced by an experimentally measurable constant, namely  $\bar{p}_{cs}$ . This makes the proposed model more usable, in terms of its calibration, as  $\bar{p}_{cs}$  can be determined through a simple undrained triaxial test (see Section 3.1 for more details).

The variation in yield surface shape in normalised  $p$  versus  $q$  stress space is shown in Figure 2 for  $\beta = 0, 0.2, 0.4$  and  $0.6$  with  $M = 1$ ,  $\bar{\rho}_e = 0.8$  and: (i)  $\bar{p}_{cs} = 0.5$  and (ii)  $\bar{p}_{cs} = 0.2$ . Figure 2 (i) also shows the evolution of the deviatoric section at  $\bar{p} = 0.5$  (only half has been shown due to symmetry) and the position of the shift stress (see Section 2.5). Note that, increasing the level of anisotropy reduces the deviatoric radius of the yield envelope, however the shape of the deviatoric section remains unchanged. The shape parameters associated with these yield surfaces are given in Table 1. For both  $\bar{p}_{cs}$  values,  $\gamma$  reduces with increasing anisotropy. However, for  $\bar{p}_{cs} = 0.5$ ,  $\alpha$  reduces whereas for  $\bar{p}_{cs} = 0.2$ ,  $\alpha$  increases with increasing anisotropy to maintain the Critical State.

| $\bar{\beta}$ | $\bar{p}_{cs} = 0.5$ |          | $\bar{p}_{cs} = 0.2$ |          |
|---------------|----------------------|----------|----------------------|----------|
|               | $\alpha$             | $\gamma$ | $\alpha$             | $\gamma$ |
| 0.0*          | 1.000                | 1.000    | 0.391                | 0.400    |
| 0.2           | 0.749                | 0.764    | 0.386                | 0.234    |
| 0.4           | 0.614                | 0.500    | 0.419                | 0.134    |
| 0.6           | 0.587                | 0.279    | 0.489                | 0.071    |

Table 1: Yield surface parameter variation with normalised anisotropy for  $\beta = 0, 0.2, 0.4$  and  $0.6$  with  $\bar{p}_{cs} = 0.5$  and  $0.2$  (\*  $\bar{\beta}$  was set to  $1 \times 10^{-5}$  to approximate  $\alpha$  when  $\bar{\beta} = 0$ ).

The yield surface of the proposed model has the following properties:

- (i) a constant Critical State stress ratio for any degree of induced anisotropy;
- (ii) a constant ratio of deviatoric yield stress above and below the axis of anisotropy independent

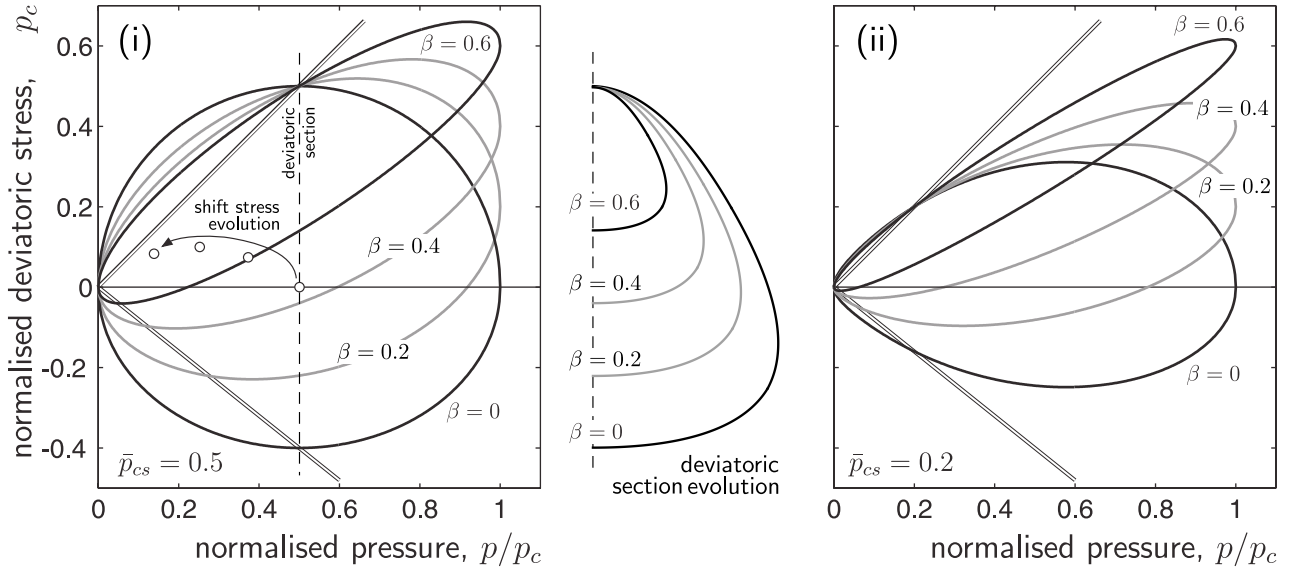


Figure 2: Yield surface shape variation with anisotropy for  $\beta = 0, 0.2, 0.4$  and  $0.6$  with  $M = 1$  and  $\bar{\rho}_e = 0.8$  for: (i)  $\bar{p}_{cs} = 0.5$  including the evolution of the deviatoric section (only half has been shown due to symmetry) (ii) and  $0.2$ .

of  $\beta_{ij}$ ;

- (iii) a narrowing of the deviatoric yield radius with increasing  $\bar{\beta}$  due to the reduction of  $\gamma$ , consistent with experimental findings on  $K_0$  consolidated soils; and
- (iv) a requirement that the level of anisotropy must be restricted to  $\beta \leq \bar{\rho}(\theta)M$ .

The final point has important implications for the evolution of anisotropy and is discussed in more detail in Section 2.5.

The uniqueness of the position of the Critical State is demonstrated in Figure 3 (i), where the dilation angle,  $\arctan(\dot{\epsilon}_v^p/\dot{\epsilon}_\gamma^p)$ , is plotted against the mobilised friction angle,  $\arctan(q/p)$ . Note that the direction of plastic flow is shown for the portion of the yield surface above the line of anisotropy. The position of isochoric plastic flow remains at a mobilised friction angle coincident with the Critical State line ( $\arctan(M)$ ). On the compressive side of the Critical State line, for a given friction angle, increasing the level of anisotropy increases the level of plastic compaction. The level of anisotropy on the dilative side of the Critical State line (mobilised friction angles greater than  $\pi/4$ ) has little influence on the dilation angle. In all cases the plastic flow direction is non associated (both in the  $p$ - $q$  plane and deviatorically).

The proposed yield surface is compared with experimental data of: (i) Tavernas *et al.* [63], (ii) Graham *et al.* [37] and (iii) Clausen *et al.* [8]. in Figure 4. In all cases the model is able to provide a reasonable fit to the data, the only significant deviation is from the data of Tavernas *et al.* [63] under triaxial extension. In that case, the model under predicts the deviatoric strength of the material, however for the same data the yield envelope provides an excellent approximation to the compression data.

## 2.5 Plastic free-energy function

Now that the yield surface and flow rule have been specified, and  $\alpha$  and  $\gamma$  related to the level of anisotropy, all that remains is the specification of laws controlling the evolution of  $p_c$  and  $\beta_{ij}$ .

Following the approach of Collins and Hilder [12], the inelastic component of the free-energy function

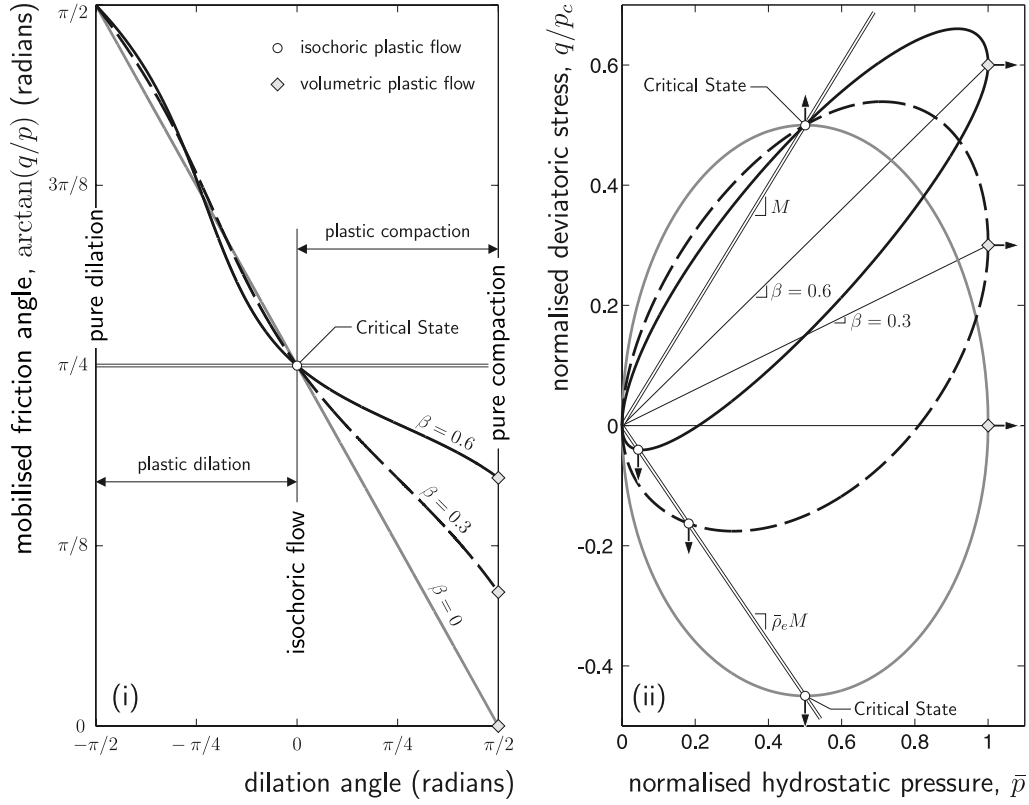


Figure 3: Direction of plastic flow: (i) dilation angle versus friction angle and (ii) associated yield surfaces for  $\bar{p}_{cs} = 0.5$ ,  $M = 1$  and  $\bar{\rho}_e = 0.9$ .

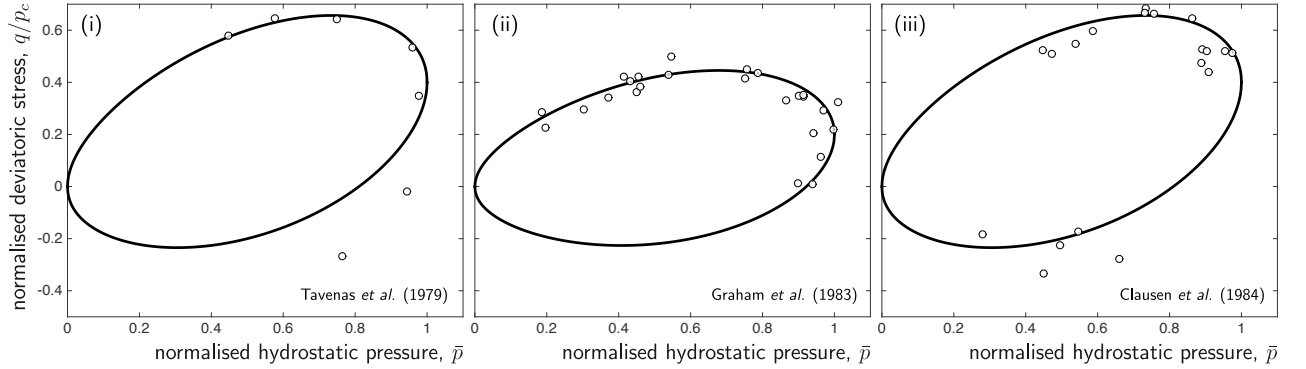


Figure 4: Yield surface comparison with experimental data: (i) Tavenas *et al.* [63], (ii) Graham *et al.* [37] and (iii) Clausen *et al.* [8].

is defined as

$$\Psi_2 = \frac{\gamma}{2}(\lambda - \kappa)p_r \exp\left(\frac{\varepsilon_v^p + f(\gamma_{ij}^p)}{\lambda - \kappa}\right), \quad (14)$$

where  $\lambda$  is the bi-logarithmic plastic compressibility index. A similar model to that presented in this paper was proposed by [20], however the model did not include the coupling between the volumetric and deviatoric plastic straining in the inelastic component of the free-energy function. This fundamental inconsistency is corrected in this paper.

Note that both  $\lambda$  and  $\kappa$  are defined in the bi-logarithmic specific volume,  $v$ , pressure,  $p$ , space. The limitations of the conventional linear relationship between specific volume (or void ratio) and the logarithm of the pre-consolidation pressure were identified by Butterfield [6]. More recently, the appropriateness of the bi-logarithmic law for finite deformation analysis was verified by [39] and used

by [69].

Taking the derivative of (14) with respect to volumetric plastic strain,  $\varepsilon_v^p$ , gives the hydrostatic component of the shift stress as

$$p^x = \frac{\partial \Psi_2}{\partial \varepsilon_v^p} = \frac{\gamma}{2} p_r \exp\left(\frac{\varepsilon_v^p + f(\gamma_{ij}^p)}{\lambda - \kappa}\right) = \frac{\gamma}{2} p_c, \quad (15)$$

where the definition of  $p_c$  is self evident. The deviatoric component of the shift stress is obtained through taking the derivative of the plastic free-energy function with respect to the deviatoric plastic strain tensor

$$s_{ij}^x = \frac{\partial \Psi_2}{\partial \gamma_{ij}^p} = \left(\frac{\partial f(\gamma_{ij}^p)}{\partial \gamma_{ij}^p}\right) p^x, \quad (16)$$

where, the derivative of  $f(\gamma_{ij}^p)$  with respect to its argument is the level of anisotropy (or shearing of the surface) and is given by

$$\frac{\partial f(\gamma_{ij}^p)}{\partial \gamma_{ij}^p} = \beta_{ij} = x_\beta \bar{r}_{ij}^\beta \left(1 - \exp(-C_\beta \varepsilon_\gamma^p)\right). \quad (17)$$

$x_\beta \bar{r}_{ij}^\beta$  is the limiting value of anisotropy that can develop under a constant stress path, with  $\bar{r}_{ij}^\beta = r_{ij}^\beta / \|r_{ij}^\beta\|$ .

### 2.5.1 Rate relationships

It is not possible to use (15) or (17) for the calculation of  $p_c$  or  $\beta_{ij}$  directly in numerical computations. This is because they require a total form of the inelastic strain that is typically not available. Instead a rate relationship must be formed for the evolution of anisotropy that can then be integrated to obtain a usable incremental relationship between inelastic strain and the hardening internal variables (the integrated form is given in Appendix B).

Assuming that  $p_c$  evolves (with plastic straining) as an independent variable and applying the chain rule to (15), the rate of evolution of the hydrostatic extent of the yield surface can be obtained as

$$\dot{p}_c = \frac{\partial p_c}{\partial \varepsilon_v^p} \dot{\varepsilon}_v^p + \frac{\partial p_c}{\partial \gamma_{ij}^p} \dot{\gamma}_{ij}^p = \frac{p_c}{\lambda - \kappa} \left(\dot{\varepsilon}_v^p + \beta_{ij} \dot{\gamma}_{ij}^p\right). \quad (18)$$

It is important to observe that introducing a deviatoric component to the shift stress (that is, including anisotropy in the yield surface) causes the rate of evolution of the extent of the yield surface to depend on the deviatoric plastic strains. This means, to maintain the concept of the Critical State, it is necessary that the level of anisotropy approaches zero when the stress state approaches the Critical State (or rather  $\beta_{ij} \dot{\gamma}_{ij} \rightarrow 0$  at the Critical State).

In addition, preserving the uniqueness of the Critical State by setting  $\alpha$  and  $\gamma$  as a function of  $\bar{p}_{cs}$  limits the level of allowable anisotropy to  $\beta < \bar{\rho}(\theta)M$ . To maintain this condition, the rate of evolution of anisotropy follows from (17) as

$$\dot{\beta}_{ij} = C_\beta \dot{\varepsilon}_\gamma^p \left(x_\beta \bar{r}_{ij}^\beta - \beta_{ij}\right). \quad (19)$$

Note, it is possible to arrive at the above equation as (17) does not explicitly depend on the stress state,  $\sigma_{ij}$ , itself but rather the deviatoric difference between the axis of anisotropy and the normalised deviatoric stress,  $\bar{r}_{ij}^\beta$ . The rate of change of this quantity with respect to stress is zero. This allows equation (19) to be obtained by considering how  $\beta_{ij}$  changes with inelastic straining.

The target level of anisotropy is controlled by  $x_\beta$  and is given by

$$x_\beta = \bar{\rho}(\theta)M \tanh(b_\beta(\bar{\eta} - 1))^2 \in [0, \bar{\rho}(\theta)M]. \quad (20)$$

$\bar{\eta} = \|r_{ij}\|/(\bar{\rho}(\theta)M)$  is the current stress ratio normalised with respect to the projected position of the Critical State envelope.  $C_\beta$  and  $b_\beta$  are material constants controlling the rate of development of anisotropy and its value under a constant  $\bar{\eta}$  stress path, respectively. The definition of  $x_\beta$  ensures that the anisotropy cannot exceed the Critical State envelope. When the stress path is outside of the Critical State the level of anisotropy in the model will tend towards the Critical State (that is, in the limit when  $\bar{\eta} \rightarrow \infty$ , the level of anisotropy will tend towards the gradient of the Critical State envelope;  $\beta/\bar{\rho}(\theta)M = 1$ ) whereas when the stress path lies within the Critical State surface the level of anisotropy is a function of the current stress ratio. However, when approaching the Critical State,  $x_\beta$  reduces to zero and consequently the anisotropy diminishes. This allows the model to arrive at a state of unbounded distortion with no change in state.  $\bar{r}_{ij}^\beta$  ensures that the anisotropy is dragged in the direction of the current stress state relative to the instantaneous position of the axis of anisotropy.

The variation in the target level of anisotropy,  $x_\beta$ , with the normalised stress ratio,  $\bar{\eta}$ , is shown in Figure 5 for three values of  $b_\beta$ , namely 0.5, 1.0 and 2.0. At the Critical State location (identified by the grey line in the figure)  $\bar{\eta} = 1$  and  $x_\beta/\bar{\rho}(\theta)M = 0$  and as  $\bar{\eta} \rightarrow \infty$ ,  $x_\beta/\bar{\rho}(\theta)M \rightarrow 1$ , this behaviour is due to the use of a hyperbolic tangent in (20). Raising the hyperbolic tangent to a power of two ensures that when  $\bar{\eta} \in [0, 1]$  the target level of anisotropy remains positive. If it was not included, for stress ratios below the Critical State, the anisotropy would evolve in the opposite direction to the stress position on the yield surface resulting in physically unrealistic results. Pre-multiplying the hyperbolic term by  $\bar{\rho}(\theta)M$  ensures that the target anisotropy is bounded by the Critical State cone and that the yield surface maintains a finite enclosing area. As shown in Figure 5, increasing  $b_\beta$  increases the target level of anisotropy, particularly in the region below the Critical State,  $\bar{\eta} \in [0, 1]$  and this can be used to control the stress path under monotonic loading such as one-dimensional consolidation.

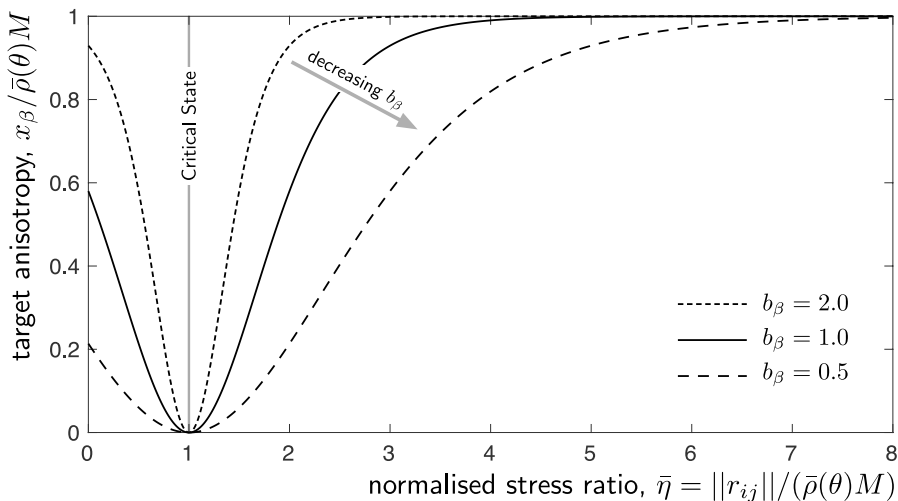


Figure 5: Variation of the target level of anisotropy,  $x_\beta$ , with the normalised stress ratio,  $\bar{\eta}$ .

It should be noted that moving on a stress path along the Critical State line there will be no evolution of anisotropy predicted by  $x_\beta$ . The definition of  $x_\beta$  is the most flexible component of the model in terms of the hyperplastic framework and (20) could be changed to a different form where this did not occur. For example, the condition where  $x_\beta = 0$  could also be governed by the hydrostatic position of the stress state in relation to the hydrostatic extent of the yield envelope. However, the purpose of the paper is to demonstrate the fundamentals of the approach and it is straightforward to replace (20) with an alternative equation for the target level of anisotropy without changing the rest of the model.

The nature of the fabric of clays at the Critical State remains a debated issue [28]. Opinions are split between those considering this asymptotic state as isotropic due to the continued rearrangement of constituents and those convinced that the state has some directional preference (anisotropy). An interested reader is referred to the work of Fu and Dafalias [31] for a micro-mechanical perspective based on discrete element analyses and that of Tejchman and Niemunis [64], again for granular materials. The model proposed here assumes that the state is isotropic to maintain internal consistency.

### 3 Physical comparisons

In this section, initially the calibration procedure for the model is presented. The model is subsequently compared with experimental data on Lower Cromer Till (LCT) and London Clay (LC). In order to present these simulations, the rate equations of the constitutive model must be integrated. Here we use an implicit stress integration approach with brief details given in Appendix B.

#### 3.1 Calibration

The nine material constants required for the anisotropic model are listed in Table 2 along with a proposed method of calibration. From this table it should be apparent that the primary test required to calibrate the model is an undrained triaxial compression test at a over consolidation ratio (OCR) of 2 following  $K_0$  consolidation and unloading. This test will allow  $G$ ,  $\alpha^e$ ,  $M$ ,  $\bar{p}_{cs}$  and  $b_\beta$  to be calibrated.  $M$  can subsequently be used to determine  $\bar{\rho}_e$  is the absence of undrained triaxial extension (UTE) test data.  $\kappa$  and  $\lambda$  can be calibrated in the standard way, albeit in bi-logarithmic void ratio, hydrostatic pressure space.

##### 3.1.1 Elastic free-energy

The constant component of the shear modulus,  $G$ , and the constant controlling the pressure-shear modulus coupling,  $\alpha^e$ , can be determined through  $K_0$  unloading (an example of this process is given in Section 3.2).

##### 3.1.2 Dissipation

An undrained triaxial compression test at a OCR of 2 following  $K_0$  consolidation and unloading will provide the gradient of the Critical State envelope under compression,  $M$ , and also the relative hydrostatic position of the Critical State,  $\bar{p}_{cs}$ .

In the absence of triaxial extension data, one can assume that the LAD coincides with the Mohr-Coulomb criterion at the compression and extension meridians. This assumption provides the normalised deviatoric radius under triaxial extension to that under triaxial compression as

$$\bar{\rho}_e = (2 + k)/(2k + 1) \quad \text{where} \quad k = (1 + \sin(\phi))/(1 - \sin(\phi)), \quad (21)$$

where the effective friction angle,  $\phi$ , can be determined from  $M$  using

$$\phi = \arcsin \left( \frac{3M}{2\sqrt{6} + M} \right). \quad (22)$$

Note that in this paper  $M$  is defined as the ratio between the deviatoric stress,  $q = \sqrt{s_{ij}s_{ij}}$  (non standard definition of  $q$ ), and the hydrostatic pressure,  $p$ .

### 3.1.3 Anisotropy

The constant controlling the developed level of anisotropy under a constant stress path,  $b_\beta$ , can be determined through one-dimensional consolidation test data. In particular, the stress ratio in  $p$  versus  $q$  stress space under continued  $K_0$  consolidation,  $\eta_{K_0}$ , can be used to specify  $b_\beta$ . Note that the following procedure for determining  $b_\beta$  is described in  $p$ - $q$  space but without loss of generality of the final result.

The key step in determining  $b_\beta$  is to arrive at the position of the stress state on the yield surface as a function of  $\eta_{K_0}$  and  $\beta_{K_0}$  that satisfies both the yield equation and the fact that

$$\frac{\dot{\varepsilon}_\gamma^p}{\dot{\varepsilon}_v^p} = \frac{\gamma(2-\gamma)(1-\bar{p})}{(\eta_{K_0} - \beta_{K_0}) - \beta_{K_0}\gamma(2-\gamma)(1-\bar{p})} = \sqrt{\frac{2}{3}}. \quad (23)$$

Due to the intimate coupling of  $\gamma$  with the level of anisotropy, it is not possible to solve directly for the hydrostatic position of the stress state on the yield surface. Instead, an iterative procedure must be used to solve for  $\beta_{K_0}$  (and therefore,  $b_\beta$ ) and  $\bar{p} = (p/p_c)$  simultaneously. Even without experimental data on  $\eta_{K_0}$ , it is possible to estimate the value of  $b_\beta$ , as demonstrated by the following.

Figure 6 demonstrates how the level of anisotropy under continued one-dimensional compression can be determined through a material's friction angle,  $\phi$ . The figure includes data from Federico *et al.* [30] (shown by discrete points), contrasted against the formula suggested by Jaky [45]. Figure 6 (i) provides a friction angle versus stress ratio under continued  $K_0$  consolidation,  $\eta_{K_0}$ , comparison, where the solid line is given by

$$\eta_{K_0} = \frac{\sqrt{6} \sin \phi}{3 - 2 \sin \phi}. \quad (24)$$

Jakys formula provides an adequate approximation to the experimental data; capturing the general trend.

Figure 6 (iii) shows the normalised hydrostatic position of the stress state on the yield surface, under this constant  $K_0$  stress path, versus friction angle. The position is shown for three different  $\bar{p}_{cs}$  values: 0.5, 0.4 and 0.3. The experimental data (discrete points linked by fine lines) show good agreement with Jaky's [45] relationship (three thick lines).

Figures 6 (ii) and (iv) compare the level of anisotropy under  $K_0$  consolidation with  $\eta_{K_0}$  and the Critical State friction angle, respectively. For the discrete points,  $\beta_{K_0}$  is determined by solving (23) for  $\beta_{K_0}$  and  $\bar{p}$  given an experimental value of  $\eta_{K_0}$ . Interestingly the normalised hydrostatic position on the yield surface,  $\bar{p}$ , has relatively little influence on the derived anisotropy except in the case of the combination of a high Critical State friction angle and a low level of anisotropy (that is, those points that are very far from the Critical State).

Figure 7 provides a calibration chart for the constant controlling the level of anisotropy under a constant stress path,  $b_\beta$ . Given a value of  $M$  and  $\eta_{K_0}$ , it is possible to obtain an approximate value of  $b_\beta$ . Relationships for two different  $\bar{p}_{cs}$  values are shown, namely  $\bar{p}_{cs} = 0.5$  and  $\bar{p}_{cs} = 0.2$ . This is shown for the case of London Clay with  $\eta_{K_0} = 0.44$  and  $M = 0.69$ , giving  $b_\beta = 2.3$ . Values for Jaky's [45] relationship between  $\eta_{K_0}$  and  $M$  are also shown by the solid grey line. Over this line the constant is restricted to  $b_\beta \in [1.6, 2.5]$  due to the relationship imposed by (24). For the region  $b_\beta > 1$ , the value of  $\bar{p}_{cs}$  has very little influence on the value of  $b_\beta$ . However, for  $b_\beta \in [0, 1]$   $\bar{p}_{cs}$  does influence the value of  $b_\beta$  required to predict the correct  $\eta_{K_0}$  value. For lower  $b_\beta$  values  $\bar{p} = p/p_c$  increases and the stress state is located closer to the hydrostatic limit of the yield surface. In this region the level of plastic dilation is strongly influence by the level of anisotropy (see Figure 3) and  $\bar{p}_{cs}$ .

## 3.2 Triaxial comparisons

This section compares the ability of the proposed model to predict the experimental behaviour of Lower Cromer Till (LCT) from the work of Gens [35]. LCT is a low plasticity glacial till with

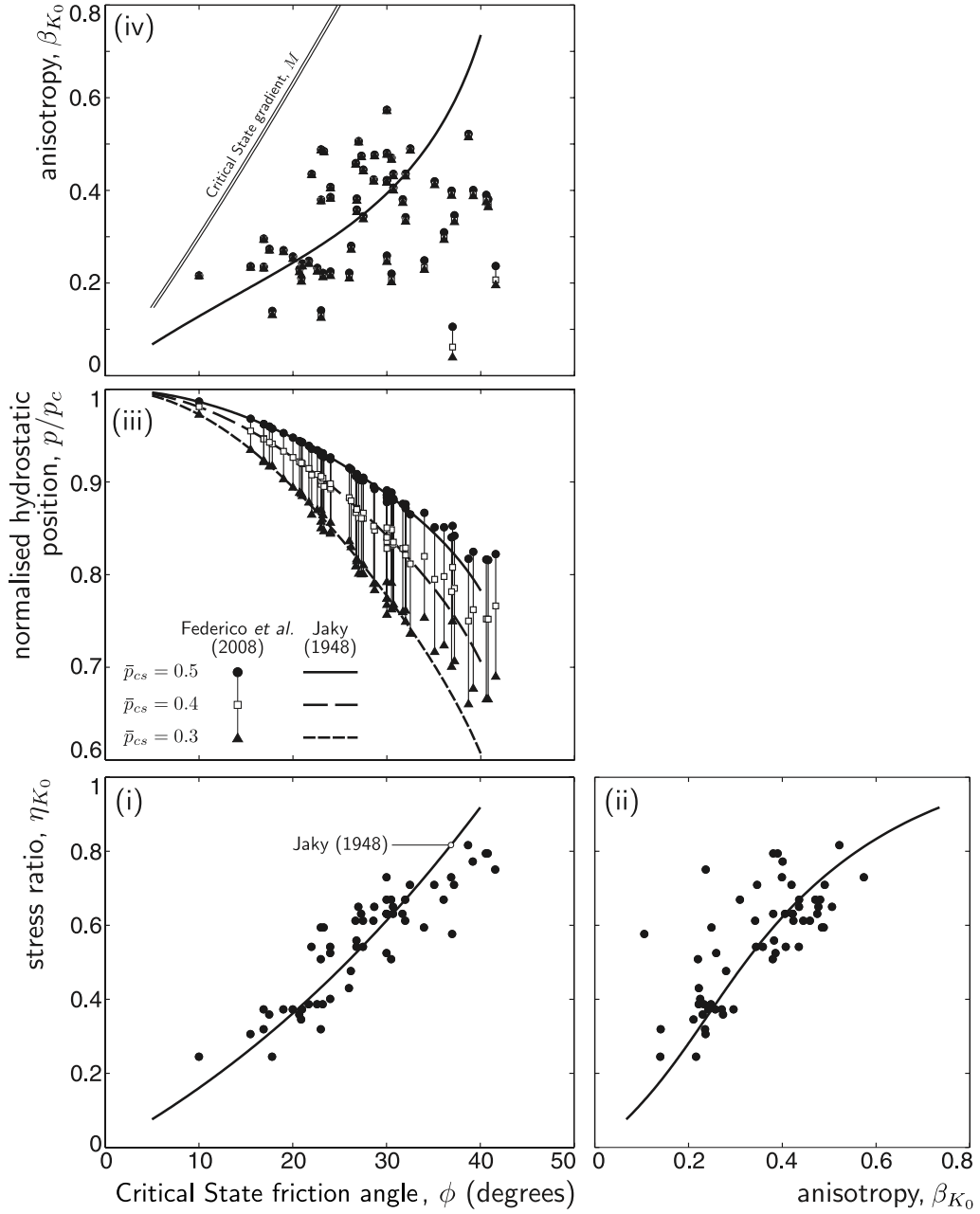


Figure 6: Anisotropy determination procedure, comparison of data from Federico *et al.* [30] (shown by discrete points) with the formula suggested by Jaky [45]: (i) stress ratio under  $K_0$  consolidation ( $\eta_{K_0}$ ) versus the Critical State friction angle ( $\phi$ , consistent with (22)), (ii)  $\eta_{K_0}$  versus anisotropy ( $\beta_{K_0}$ ), (iii) normalised hydrostatic position on the yield surface ( $p/p_c$ ) versus  $\phi$  and (iv)  $\beta_{K_0}$  versus  $\phi$ , where the Critical State gradient is also shown.

high natural variability, classified as a low-plasticity sandy silty-clay. All of the experimental tests presented by Gens [35] were from reconstituted samples with a specific weight of 2.65. The mineralogy of these samples was comprised of principally quartz with minor proportions of calcite, feldspar and clay minerals. The clay fraction was mainly composed of calcite and illite with smaller components of smectite, kaolinite and chlorite. The material had a liquid limit, plastic limit and plasticity index of 25, 13 and 12 respectively. Approximately 17% of the material was clay (giving an activity of 0.716), the remainder was mainly composed of sand, with very little silt.

Figure 8 compares the experimental data with the proposed model ((i) to (iv)) with SANIclay [26] ((v) to (viii)) and the rotational hardening model of Yang *et al.* [71] ((vii) and (viii)) under one-

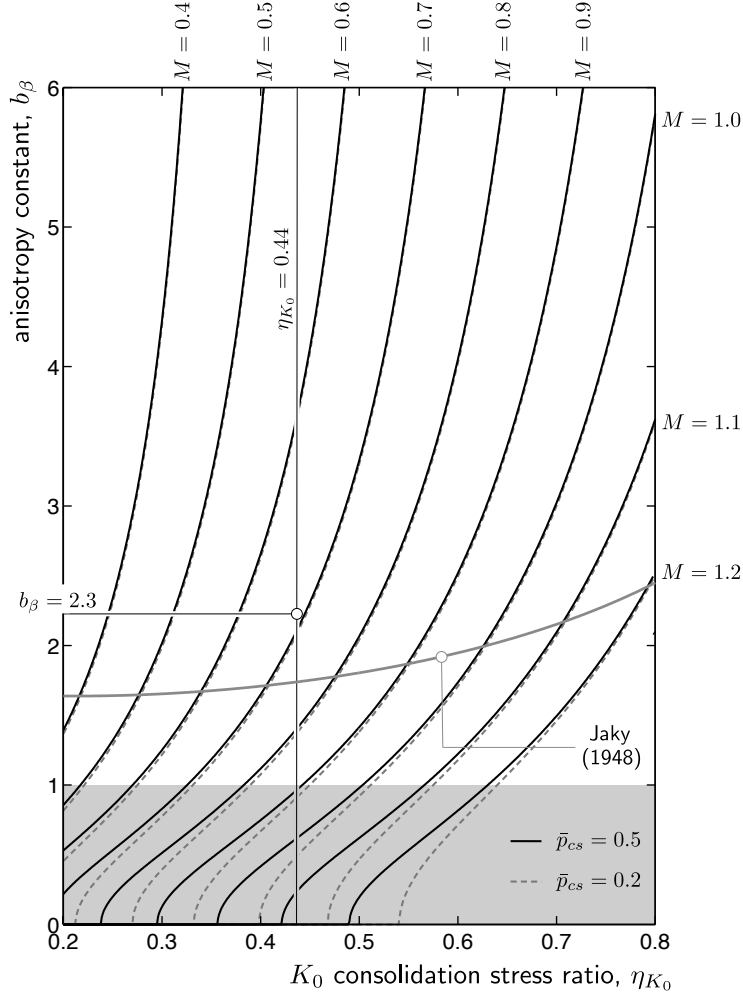


Figure 7: Calibration chart for  $b_\beta$  based on the gradient of the Critical State,  $M$ , and the stress ratio under  $K_0$  consolidation,  $\eta_{K_0}$ . Relationships for two different  $\bar{p}_{cs}$  values are shown.

dimensional consolidation ((i) and (v)) and swelling ((ii) and (vi)), followed by undrained triaxial compression ((iii) and (vii)) or extension ((iv) and (viii)). The constants for the proposed model were set as:  $\kappa = 0.007$ ,  $G_0 = 2\text{MPa}$ ,  $\alpha^e = 75$ ,  $\lambda = 0.044$ ,  $M = 0.96$ ,  $\bar{p}_{cs} = 0.45$ ,  $\bar{p}_e = 0.73$ ,  $C_\beta = 80$  and  $b_\beta = 2$ . The stress paths for SANIclay were obtained from [26], where the eight constants required for the model were calibrated on the same LCT experimental data as used in this paper. Unfortunately, the paper did not present the full one-dimensional loading and unloading behaviour of the model. The portions of the paths presented in that paper have been reproduced in Figure 8 (v) and (vi). It appears that, unlike the work in this paper, [26] allowed their model to start at a stress state in agreement with the experimental data for each of the individual triaxial simulations rather than simulating the material's full stress history. The stress paths for the model of Yang et al. [71] have been reproduced for the undrained triaxial compression and tension tests, again their model was calibrated on the same dataset, [35], as used in this paper. For comparisons of the LCT data with other constitutive models the reader is referred to [70].

The one-dimensional drained compaction followed by unloading of LCT (discrete points) is compared with the numerical prediction of the proposed model (solid line) in Figures 8 (i) and (ii). The proposed constitutive model started from a hydrostatic stress and isotropic material state with a reference pressure and size of the yield surface of 75kPa. The model was then subjected to a one-dimensional compressive strain path in increments of  $\Delta\varepsilon_z = 1 \times 10^{-4}$  to a pressure of 233kPa followed by unloading to 62kPa. The model offers reasonable agreement with the experimental data under

|               | constant       |   | calibration   | default |
|---------------|----------------|---|---|---------|
| elastic       | $\kappa$       | bi-logarithmic elastic compressibility index                          | unload-load hydrostatic consolidation test                              | -       |
|               | $G$            | constant shear modulus  | stress path of 1D unloading following $K_0$ consolidation               | 2 MPa   |
|               | $\alpha^e$     | pressure-shear modulus coupling                                       |   | 0       |
| yield surface | $\lambda$      | bi-logarithmic plastic compressibility index                          | virgin hydrostatic consolidation  | -       |
|               | $M$            | gradient of the Critical State line                                   | undrained triaxial compression  | -       |
|               | $\bar{p}_{cs}$ | normalised hydrostatic position of the yield surface-CSL intersection | undrained triaxial compressive test at an OCR of 2                      | 0.5     |
|               | $\bar{\rho}_e$ | normalised extension deviatoric radius                                | undrained triaxial extension test (or determined from $M$ )             | (21)    |
| anisotropic   | $b_\beta$      | target anisotropy under constant stress path                          | $\eta_{K_0}$ under a $K_0$ consolidation test (or determined from $M$ ) | Fig 7   |
|               | $C_\beta$      | rate of development of anisotropy                                     | 1D swelling   | 40      |

Table 2: Material constants for the anisotropic model split into constants associated with the model’s: (i) elastic behaviour, (ii) yield surface and (iii) development of anisotropy.

both (i) loading between A and B and (ii) unloading, B to D. Between B and C the model predicts elastic behaviour. The onset of yield occurs at C and the model’s response has a notable change in gradient until arriving at D.

The behaviour of the proposed model under undrained triaxial compression and extension is shown in Figures 8 (iii) and (iv). The model started from the stress and material parameter state obtained from the one-dimensional loading and unloading simulation (point D) and was subjected to a strain increment with the following non-zero components:  $\Delta\varepsilon_z = \pm 1 \times 10^{-4}$ ,  $\Delta\varepsilon_x = \mp 0.5 \times 10^{-4}$  and  $\Delta\varepsilon_y = \mp 0.5 \times 10^{-4}$ . The simulation continued along this strain path until the model reached a constant stress state on the Critical State surface with zero anisotropy. The proposed model shows good agreement with the experimental data for undrained triaxial compression whereas the SANIclay model and the model of Yang et al. [71], due to their ellipsoid-shaped yield surfaces and the form of elasticity employed, over-predict the deviatoric stress prior to arriving at the Critical State. In particular the model of Yang et al. [71] significantly over predicts the length of the elastic part of the stress response, only yielding at E”. The final state of the model, F”, has an error of almost 50% (or 54kPa) in terms of the deviatoric stress at the Critical State. However, all of the models capture the general trends observed in the experimental data.

Under undrained triaxial extension, the SANIclay model predicts an incorrect stress path direction and arrives at the Critical State with an error of 52kPa (or 55%) in the final hydrostatic stress state at H’. The prediction of the model of Yang et al. [71] shows the correct general trends and,

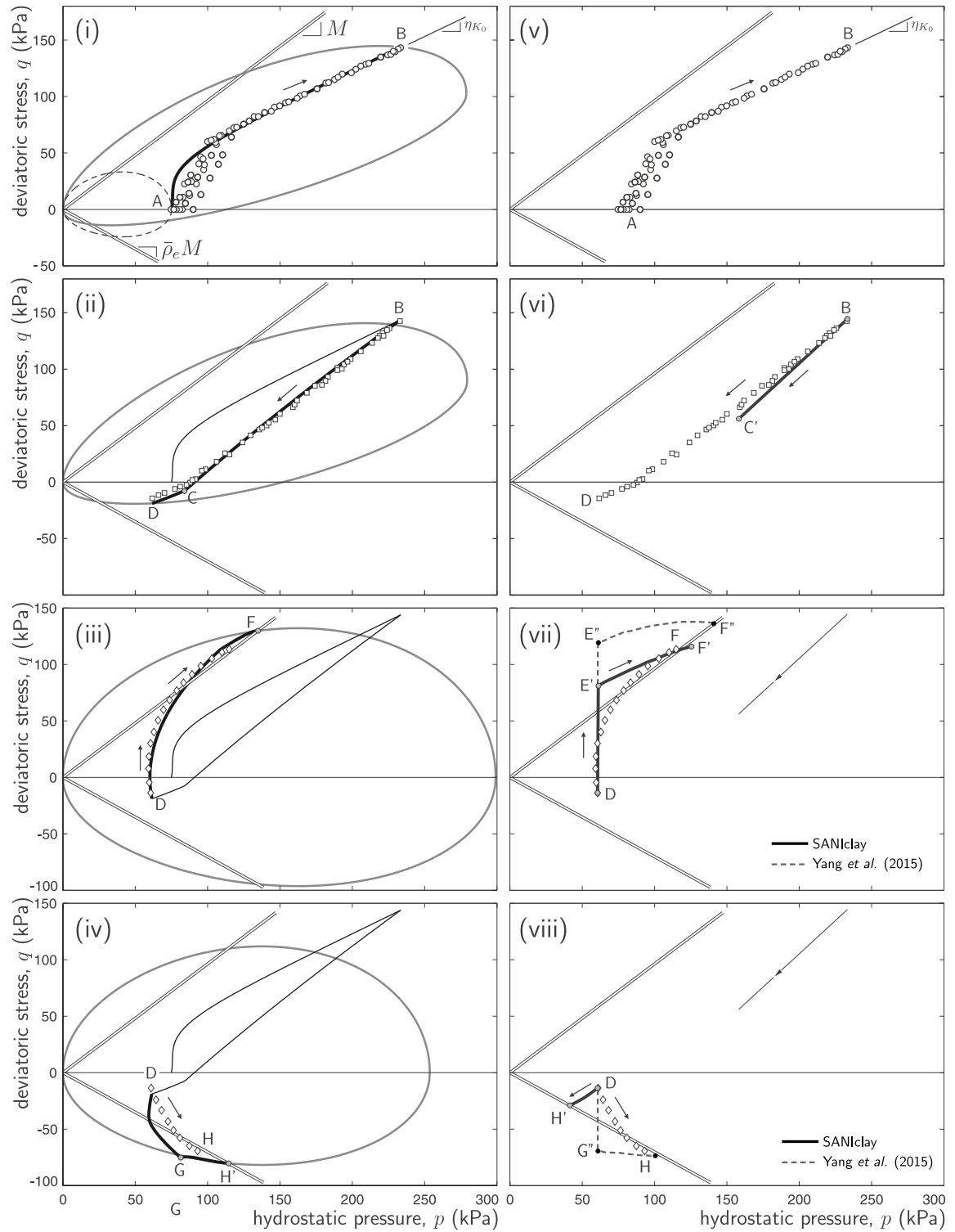


Figure 8: Comparison of the proposed model ((i) to (iv)) with SANIclay [26] ((v) to (viii)) and the rotational hardening model of Yang et al. [71] ((vii) and (viii)) under one-dimensional consolidation ((i) and (v)) and swelling ((ii) and (vi)) followed by undrained triaxial compression ((iii) and (vii)) or extension ((iv) and (viii)).

despite over-predicting the length of the elastic portion of the stress path and only yielding at  $G''$ , arrives at a final state on the CSL in reasonable agreement with the experimental data at  $H$ . The proposed model predicts a more realistic initial stress path direction, albeit with an overestimating the deviatoric shear stress until point  $G$  where there is an abrupt change in the stress path direction.

This change is due to the axis of anisotropy moving through the hydrostatic axis. Between D and G, the level of anisotropy in the yield surface reduces, being dragged towards the stress state inside the Critical State surface. This reduction causes an increase in the shape parameters  $\alpha$  and  $\gamma$ , thereby increasing the deviatoric extent of the yield surface. Overall, the proposed model, when compared with the SANIclay and Yang et al. [71] models, provides a more realistic and complete representation of the material behaviour of LCT during the tests considered.

### 3.3 Hollow cylinder analysis

This section presents finite-element simulations of a hollow cylinder test on London Clay (LC). LC is categorised as a stiff, fissured, heavily overconsolidated clay of high plasticity. LC has undergone significant experimental investigation and computational analysis since the 1950s (see [53] and [52] and the references contained within) as a consequence of its engineering importance with regard to deep foundation design and underground excavations in the UK's capital city. LC is mainly composed of Illite and Montmorillonite minerals, with smaller fractions of Kaolinite. The clay fraction of LC is typically between 40% and 60% with a plasticity index of between 40 and 70 (depending on location) [52]. Due to its brittle nature, LC poses a challenge for models based on the concept of the Critical State as it tends to rupture before reaching an asymptote.

Before considering the hollow cylinder apparatus (HCA) tests, the proposed model was calibrated using hydrostatic consolidation/swelling and undrained triaxial test data. The comparison of the model response with the test data is shown in Figure 9. The hydrostatic consolidation (A to B, black-filled circles) and swelling (B to C, white-filled squares) test data and the model's response (solid black line) are shown in Figure 9 (i). The model shows excellent agreement for this trivial, easy to calibrate, test. The constants for the proposed model were:  $\kappa = 0.024$ ,  $G_0 = 2\text{MPa}$ ,  $\alpha^e = 25$ ,  $\lambda = 0.073$ ,  $M = 0.69$ ,  $\bar{p}_{cs} = 0.45$ ,  $\bar{\rho}_e = 0.90$ ,  $C_\beta = 20$  and  $b_\beta = 2.3$ .

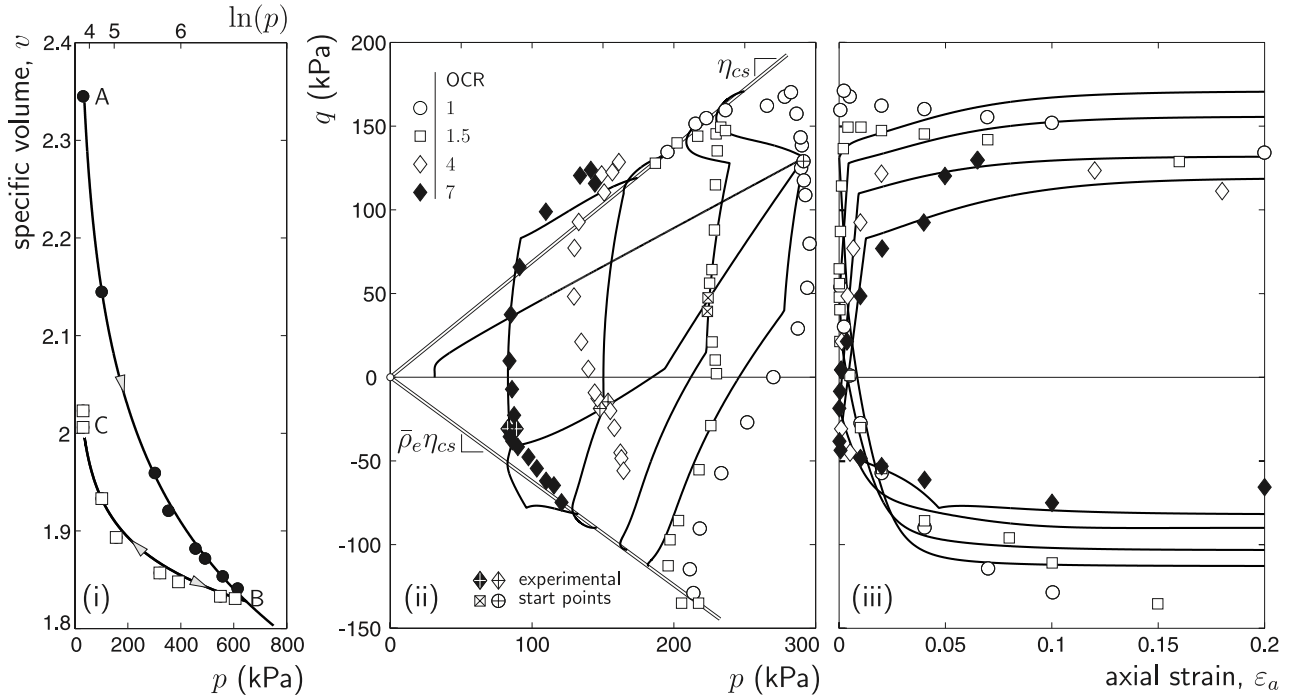


Figure 9: London Clay calibration: (i) hydrostatic consolidation and swelling comparison with data (shown by discrete points) from Gasparre [34]. UTC and UTE following K0 consolidation and swelling comparison with experimental data from Hight *et al.*[40] (original data from Jardine *et al.* [46]): (ii) stress path in  $p$ - $q$  space and (iii) axial strain-deviatoric stress response.

A comparison of the UTC and UTE response following K0 consolidation and swelling is shown in

Figures 9 in terms of: (ii) stress path in p-q space and (iii) axial strain-deviatoric stress response. The model provides good agreement with the starting points of the triaxial compression and extension tests (shown by the *crossed* symbols) for all of the overconsolidation ratios. However, the fit to the undrained triaxial experimental data is only adequate, albeit capturing the general trends. The model appears to be better at capturing the heavily overconsolidate soil behaviour rather than those tests conducted in the normally to lightly overconsolidated region. The material constants for based on this calibration were then used to simulate the undrained HCA tests on LC (without modification of constants).

Nishimura and co-workers [52, 53] presented a series of undrained HCA tests on LC from undisturbed block samples. The HCA allows independent control of four stress components, namely the axial,  $\sigma_z$ , circumferential,  $\sigma_\theta$ , radial,  $\sigma_r$ , and the shear stress in the  $z - \theta$  plane,  $\sigma_{z\theta}$ . This is achieved through the application of an axial load,  $W$ , a torque,  $M_T$ , an internal,  $p_i$ , and an external,  $p_o$ , pressure to a hollow cylindrical sample of length  $l$  internal radius  $r_i$  and external radius  $r_o$ . A schematic of the HCA is shown in Figure 10 (i). The tests were conducted with an aim to achieve the following conditions

- (i) constant total pressure,  $p_t$  (that is, the sum of the effective pressure,  $p$ , and the pore water pressure,  $u$ );
- (ii) constant intermediate principal stress ratio throughout the loading path

$$b = \frac{\sigma_2 - \sigma_3}{\sigma_1 - \sigma_3}; \quad \text{and} \quad (25)$$

- (iii) constant stress path with

$$\frac{\sigma_z - \sigma_\theta}{2} = \frac{\sigma_{z\theta}}{\tan(2\alpha_{d\sigma})}, \quad (26)$$

where  $\sigma_z$  is the axial stress,  $\sigma_\theta$  the circumferential stress,  $\sigma_{z\theta}$ , the shear stress in the  $z - \theta$  plane (as seen in Figure 10 (ii)) and  $\alpha_{d\sigma}$  is the incremental stress path direction.

These three conditions (together with the starting stress condition) allow determination of the idealised, uniform, stress state for the undrained HCA experiments. Assuming that the radial stress is the intermediate principal stress (as shown in Figure 10 (iii)) and using the condition of constant pressure, we can obtain the radial stress as

$$\sigma_r = p_t + \frac{4(b - 1/2)\sigma_{z\theta}\sqrt{\tan(2\alpha_{d\sigma})^{-2} + 1}}{3}. \quad (27)$$

From the total mean stress,  $p_t$ , and (26), the axial and circumferential stresses follow as

$$\sigma_\theta = \frac{3p_t - \sigma_r}{2} - \frac{\sigma_{z\theta}}{\tan(2\alpha_{d\sigma})} \quad \text{and} \quad \sigma_z = 3p_t - \sigma_r - \sigma_\theta. \quad (28)$$

These constant stress path tests can be driven by the applied shear stress,  $\sigma_{z\theta}$ , with the other normal stresses subsequently calculated from (27) and (28), once the total mean stress ( $p_t$ ), intermediate principal stress ratio ( $b$ ) and stress path direction ( $\alpha_{d\sigma}$ ) have been specified. Note that (27) and (28) require the specification of a value for  $\sigma_{z\theta}$ . For tests AC6705, AC4505 and AC2305, setting  $\sigma_{z\theta} = 1$  allows increment in the normal stress components relative to a unit increase in the shear stress to be determined. In the case of AC9005 and AC0005,  $\sigma_{z\theta} = 0$ .

[52] identified the tests using a two-character, four-number format. For example, AC9005 is a test on an anisotropically consolidated sample (AC) with  $\alpha_{d\sigma} = 90^\circ$  and  $b = 0.5$ . Here we will only consider the AC tests with principal stress ratio of 0.5. Analysis of the HCA tests, as performed experimentally by [52], can be split into four stages:

- (i) *In-situ* stress path (experimental tests were conducted on samples taken from a current *in-situ* depth of 16.3m) following three geological events [52]:
  - (a) deposition of 175m of LC with a bulk unit weight of  $19.8\text{kN/m}^3$  simulated by the drained one-dimensional consolidation to a vertical stress of 3.673MPa;
  - (b) erosion of the 175m over-burden simulated by the drained one-dimensional unloading to a vertical stress of 208kPa; and
  - (c) deposition of terrace gravel of bulk unit weight  $19.1\text{kN/m}^3$  to a depth of 5.8m simulated by the drained one-dimensional consolidation to a vertical stress of 319kPa.
- (ii) Shift the current stress state to the assumed *in-situ* stress conditions of an effective pressure  $p = 323\text{kPa}$  and a stress state off the hydrostatic axis with  $(\sigma_z - \sigma_\theta) = -165\text{kPa}$  and  $\sigma_\theta = \sigma_r$ .
- (iii) An undrained change in the intermediate principal stress ratio, from an initial value of 1, to the required  $b$  value along the stress path

$$\{\Delta\sigma_r \quad \Delta\sigma_\theta \quad \Delta\sigma_z\} = \Delta\sigma\{-2 \quad 1 \quad 1\},$$

following a Tresca meridian in principal stress space, such that total pressure (set at 573kPa with a pore pressure of 250kPa) and  $(\sigma_z - \sigma_\theta)$  remain constant. Changing  $b$  from 1 to 0.5 requires  $\Delta\sigma = 27.5\text{kPa}$ .

- (iv) Undrained shear with a constant total pressure and constant  $b$  along a fixed  $\alpha_{d\sigma}$  stress path, with the normal stress components obtained from (27) and (28).

All stages were conducted using a single eight-noded hexahedral finite-element, stages one and two assumed drained conditions whereas in the subsequent stages undrained conditions were imposed with the boundary conditions and loading as shown in Figure 10 (iv). These boundary conditions result in a uniform stress (and strain) distribution through the element.

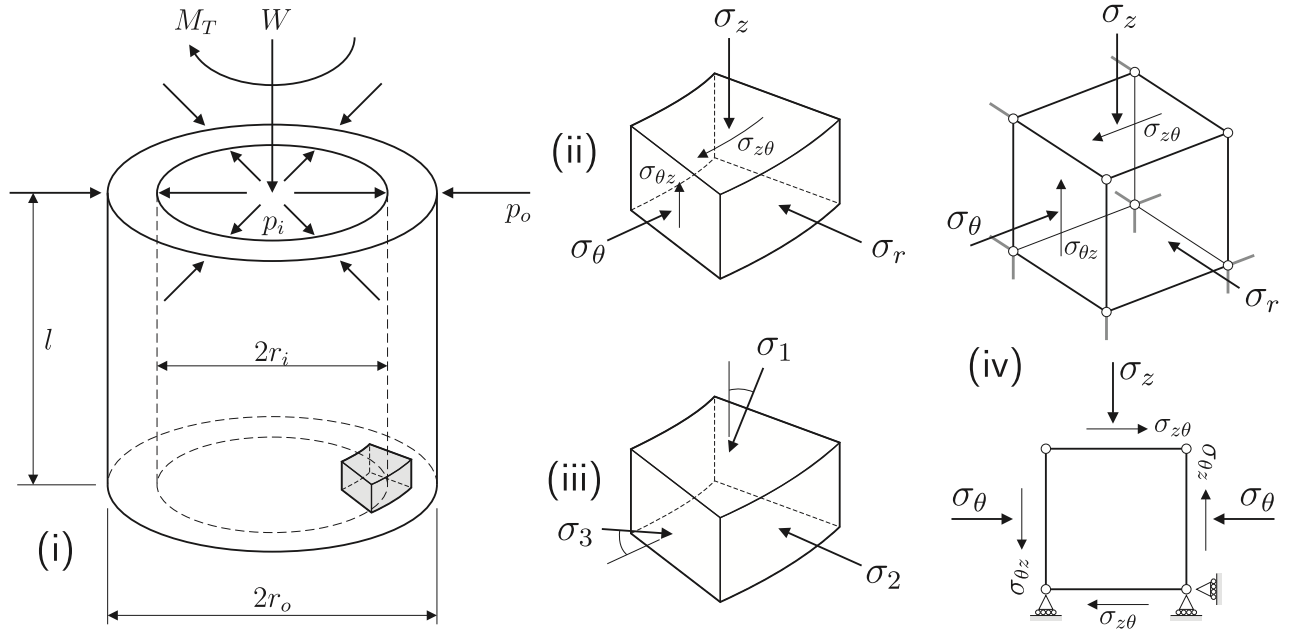


Figure 10: Hollow cylinder apparatus: (i) applied loads and pressures, (ii) average internal stresses, (iii) principal stresses and (iv) single eight-noded hexahedral finite-element: loading and boundary conditions (reproduced from [18]).

Note, that as the primary variable in a constitutive model is the applied strain, a finite-element implementation is required to simulate these stress-controlled hollow cylinder tests to allow the internal stress in the constitutive model to be brought into equilibrium with the externally applied

tractions (representing the applied stresses in the test). The finite-element code used in this study essentially has the same format as that presented by [22], albeit without the inclusion of geometric non-linearity. The constitutive model was implemented using a fully implicit backward-Euler algorithm including the derivation of the algorithmic consistent tangent (see the work of [61]) to ensure asymptotic quadratic convergence of the global non-linear finite-element iterations. Full details of the adopted framework can be found in [18] and the algorithmic implementation of the model is covered in Appendix B of this paper. Note that in this case only a single element (as shown in Figure 10 (iv)) is required to solve the simulation as the boundary conditions are applied in such a way that at all steps in the analysis the stress does not vary through the element.

The principal stress deviator versus principal strain deviator response of the single-surface anisotropic model is shown, and compared with experimental data, in Figure 11. The response of the modified Cam-clay (MCC) is also shown. The material constants for the MCC model were set as follows:  $\kappa = 0.024$ ,  $\lambda = 0.073$ ,  $G = 18\text{MPa}$  (pressure insensitive),  $M = 0.69$  and  $\bar{\rho}_e = 0.90$ . The proposed model response (shown by the continuous line) shows reasonable agreement with the experimental data for all of the stress paths. However, the MCC model response (shown by the dashed line) significantly over estimates the stress deviator in all cases.

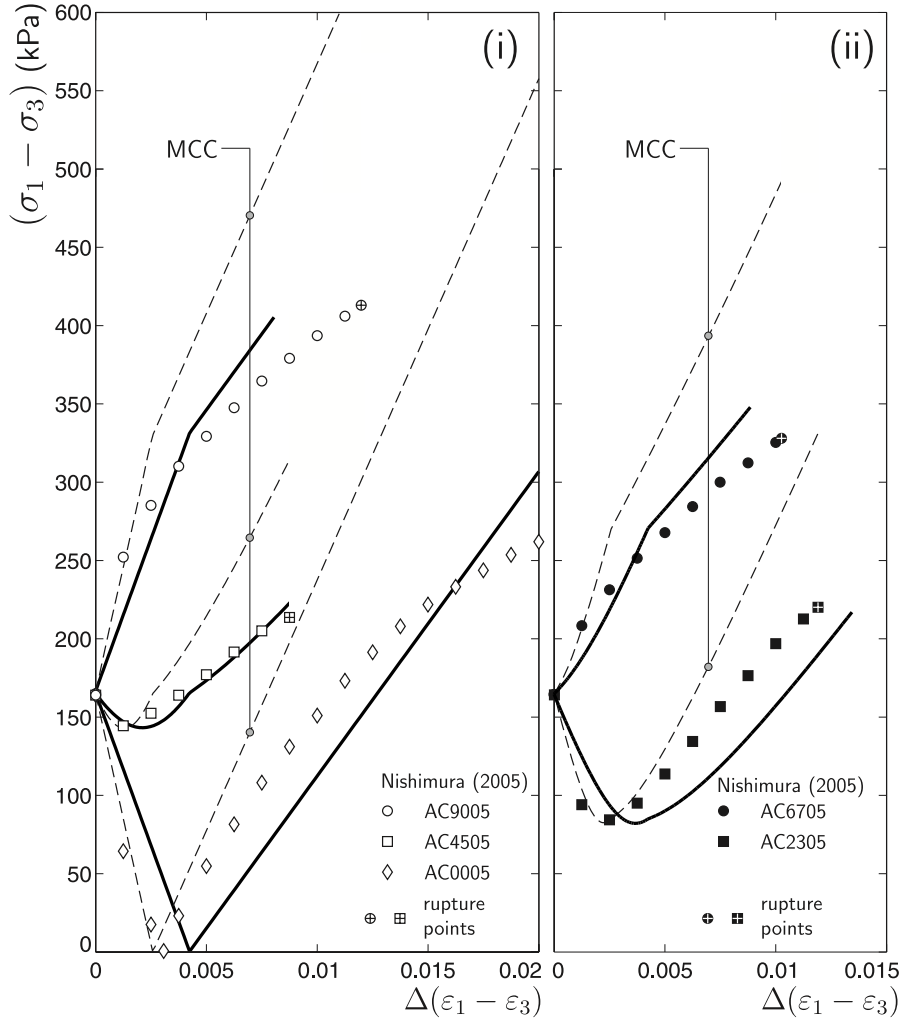


Figure 11: Principal stress deviator versus principal strain deviator comparison of experimental data (shown by discrete points) with the anisotropic model (solid line) and MCC (dashed line) for the HCA analyses: (i) AC9005, AC9045 and AC0005 and (ii) AC6705 and AC2305.

## 4 Conclusions

This paper has presented the motivation behind and the theoretical of development of a single surface anisotropic hyperplasticity model. The model extends the isotropic family of models developed by [19], resulting in a model that offers: (i) a measure of anisotropy represented by a degree of induced anisotropic shearing of the yield surface off the hydrostatic axis; (ii) a more physically realistic pressure sensitive elastic free energy function resulting in both a pressure sensitive bulk and shear modulus; (iii) a method to specify the yield surface shape parameters based on a single *experimentally measurable* constant; (iv) a unique Critical State surface throughout the loading process regardless of the level of induced anisotropy; and (v) a convex yield envelope, invariant to the level of anisotropy or the selected LAD. One limitation of the model is that it is not able reproduce shear modulus degradation with small shear strain cycles due to the adopted hyperelastic behaviour inside the yield envelope. The proposed model was compared with the SANIclay model [26] and the recently proposed model of Yang et al. [71], giving a more realistic representation of the material behaviour of LCT [35] during the tests considered.

The model was also compared with experimental data from hollow cylinder tests on LC. The entire stress history of the HCA LC samples was simulated using a single set of material constants, from deposition, through erosion to re-burial and subsequent lab-based undrained shearing. This has seldom been attempted in the past but is essential to convincingly demonstrate the ability of a model to predict observed experimental behaviour.

## References

- [1] J. Argyris, G. Faust, J. Szimmat, E. Warnke, and K. Willam. Recent developments in the finite element analysis of prestressed concrete reactor vessels. *Nuclear Engineering and Design*, 28(1): 42–75, 1974.
- [2] J. Bardet. Lode dependences for isotropic pressure-sensitive elastoplastic materials. *Transactions of the ASCE*, 57(3):498–506, 1990.
- [3] G. Belokas and M. Kavvas. An anisotropic model for structured soils part i: theory. *Computers and Geotechnics*, 37(6):737–747, 2010.
- [4] S. Bhowmik and J. Long. A general formulation for the cross sections of yield surfaces in octahedral planes. In G. Pande and J. Middleton, editors, *NUMENTA 90*, pages 795–803, 1990.
- [5] R. Borja, C. Tamagnini, and A. Amorosi. Coupling plasticity and energy-conserving elasticity models for clays. *Journal of Geotechnical and Geoenvironmental Engineering*, 123(10):948–957, 1997.
- [6] R. Butterfield. A natural compression law for soils (an advance on e-logp’). *Géotechnique*, 29 (4):469–480, 1979.
- [7] A. Casagrande. *Contributions to soil mechanics*, chapter Characteristics of cohesionless soils affecting the stability of slopes and earth fills, pages 257–276. Boston Society of Civil Engineers, 1936.
- [8] C.-J. F. Clausen, J. Graham, and D. M. Wood. Yielding in soft clay at Mastemyr, Norway. *Géotechnique*, 34(4):581–600, 1984.
- [9] I. Collins. A systematic procedure for constructing critical state models in three dimensions. *International Journal of Solids and Structures*, 40(17):4379–7397, 2003.
- [10] I. Collins. Elastic/plastic models for soils and sands. *International Journal of Mechanical Sciences*, 47(4-5):493–508, 2005.
- [11] I. Collins. The concept of stored plastic work or frozen elastic energy in soil mechanics. *Géotechnique*, 55(5):373–382, 2005.
- [12] I. Collins and T. Hilder. A theoretical framework for constructing elastic/plastic constitutive models of triaxial tests. *Int. J. Numer. Anal. Meth. Geomech.*, 26(13):1313–1347, 2002.
- [13] I. Collins and G. Houlsby. Application of thermomechanical principles to the modelling of

- geotechnical materials. *Proc. R. Soc. Land. A*, 453:1975–2001, 1997.
- [14] I. Collins and P. Kelly. A thermomechanical analysis of a family of soil models. *Géotechnique*, 52(7):507–518, 2002.
- [15] I. Collins and B. Muhunthan. On the relationship between stress-dilatancy, anisotropy, and plastic dissipation for granular materials. *Géotechnique*, 53(7):611–618, 2003.
- [16] I. Collins, B. Muhunthan, A. Tai, and M. Pender. The concept of a reynoldstaylor state and the mechanics of sands. *Géotechnique*, 57(5):437–447, 2007.
- [17] I. Collins, B. Muhunthan, and B. Qu. Thermomechanical state parameter models for sands. *Géotechnique*, 60(8):611–622, 2010.
- [18] W. Coombs. *Finite deformation of particulate geomaterials: frictional and anisotropic Critical State elasto-plasticity*. PhD thesis, Durham University, 2011.
- [19] W. Coombs and R. Crouch. Algorithmic issues for three-invariant hyperplastic critical state models. *Comput. Methods Appl. Mech. Engrg.*, 200(25-28):2297–2318, 2011.
- [20] W. M. Coombs. Unique critical state single-surface anisotropic hyperplasticity. In *XII International Conference on Computational Plasticity. Fundamentals and Applications. COMPLAS XII*, 2013.
- [21] W. M. Coombs and R. S. Crouch. Non-associated reuleaux plasticity: analytical stress integration and consistent tangent for finite deformation mechanics. *Comput. Methods Appl. Mech. Engrg.*, 200(9-12):1021–1037, 2011.
- [22] W. M. Coombs, R. S. Crouch, and C. E. Augarde. 70-line 3d finite deformation elastoplastic finite-element code. In T. Benz and S. Nordalm, editors, *7th European Conference on Numerical Methods in Geotechnical Engineering (NUMGE)*, pages 151–156, Trondheim, Norway, June 2010.
- [23] W. M. Coombs, R. S. Crouch, and C. E. Augarde. Reuleaux plasticity: analytical backward Euler stress integration and consistent tangent. *Comput. Methods Appl. Mech. Engrg.*, 199(25-28):1733–1743, 2010.
- [24] W. M. Coombs, R. S. Crouch, and C. E. Augarde. A unique critical state two-surface hyperplasticity model for fine-grained particulate media. *Journal of the Mechanics and Physics of Solids*, 61(1):175–189, 2013.
- [25] Y. Dafalias. Bounding surface plasticity. i: Mathematical foundation and hypoplasticity. *Journal of Engineering Mechanics ASCE*, 112(9):966–987, 1986.
- [26] Y. Dafalias, M. Manzari, and A. Papadimitriou. SANICLAY: simple anisotropic clay plasticity model. *Int. J. Numer. Anal. Meth. Geomech.*, 30(12):1231–1257, 2006.
- [27] Y. F. Dafalias and M. Taiebat. Anatomy of rotational hardening in clay plasticity. *Géotechnique*, 63(16):1406–1418, 2013.
- [28] Y. F. Dafalias and M. Taiebat. Rotational hardening with and without anisotropic fabric at critical state. *Géotechnique*, 64(6):507–511, 2014.
- [29] H. A. M. v. Eekelen. Isotropic yield surfaces in three dimensions for use in soil mechanics. *Int. J. Numer. Anal. Meth. Geomech.*, 4(1):89–101, 1980.
- [30] A. Federico, G. Elia, and V. Germano. A short note on the earth pressure and mobilized angle of internal friction in one-dimensional compression of soils. *Journal of GeoEngineering*, 3(1):41–46, 2008.
- [31] P. Fu and Y. Dafalias. Fabric evolution within shear bands of granular materials and its relation to critical state theory. *Int. J. Numer. Anal. Meth. Geomech.*, 35:1918–1948, 2011.
- [32] A. Gajo and D. Bigoni. A model for stress and plastic strain induced nonlinear, hyperelastic anisotropy in soils. *Int. J. Numer. Anal. Meth. Geomech.*, 32(7):833–861, 2008.
- [33] A. Gajo and D. Wood. A new approach to anisotropic, bounding surface plasticity: general formulation and simulations of natural and reconstituted clay behaviour. *Int. J. Numer. Anal. Meth. Geomech.*, 25(3):207–214, 2001.
- [34] A. Gasparre. *Advanced Laboratory Characterisation of London Clay*. PhD thesis, Imperial College London, July 2005.
- [35] A. Gens. *Stress-strain Characteristics of a low plasticity clay*. PhD thesis, Imperial College of Science and Technology, Univeristy of London, November 1982.

- [36] A. Gens and D. Potts. Critical state models in computational geomechanics. *Eng. Comput.*, 5(3):178–197, 1988.
- [37] J. Graham, M. L. Noonan, and K. V. Lew. Yield states and stress-strain relationships in a natural plastic clay. *Can. Geotech. J.*, 20(3):502–516, 1983.
- [38] G. Gudehus. Elastoplastische stoffgleichungen für trockenen sand. *Ingenieur-Archiv*, 42(3):151–169, 1973.
- [39] K. Hashiguchi. Verification of compatibility of isotropic consolidation characteristics of soils to multiplicative decomposition of deformation gradient. *Soils and Foundations*, 48(4):597–602, 2008.
- [40] D. Hight, F. McMillan, J. Powell, R. Jardine, and C. Allenou. Some characteristics of london clay. In T. *et al.*, editor, *Characterisation of Engineering Properties of Natural Soils*, 2003.
- [41] G. Houlsby. *A Study of Plasticity Theories and Their Applicability to Soils*. PhD thesis, University of Cambridge, 1981.
- [42] G. Houlsby. The use of a variable shear modulus in elastic-plastic models for clays. *Computers and Geotechnics*, 1(1):3–13, 1985.
- [43] G. Houlsby and A. Puzrin. A thermomechanical framework for constitutive models for rate-independent dissipative materials. *International Journal of Plasticity*, 16(9):1017–1047, 2000.
- [44] G. Houlsby and A. Puzrin. *Principles of Hyperplasticity*. Springer-Verlag London Limited, 2006.
- [45] J. Jaky. Pressure in silos. In *Proceedings of the 2nd International Conference on Soil Mechanics and Foundation Engineering*, volume 1, pages 103–107, June 21-30 1948.
- [46] R. Jardine, M. Symes, and J. Burland. The measurement of soil stiffness in the triaxial apparatus. *Géotechnique*, 34(3):323–340, 1984.
- [47] M. Karstunen and M. Koskinen. Plastic anisotropy of soft reconstituted clays. *Canadian Geotechnical Journal*, 45(3):314–328, March 2008.
- [48] M. Karstunen, H. Krenn, S. Wheeler, M. Koskinen, and R. Zentar. Effect of anisotropy and destructuration on the behavior of murro test embankment. *International Journal of Geomechanics ASCE*, 5(2):87–97, 2005.
- [49] P. Lade and J. Duncan. Elastoplastic stress-strain theory for cohesionless soil. *ASCE Journal of the Geotechnical Engineering Division*, 13(11):1037–1053, 1975.
- [50] H. Matsuoka and T. Nakai. Stress-deformation and strength characteristics of soil under three different principal stresses. *Proc. JSCE*, 232:59–70, 1974.
- [51] G. Maugin. *The Thermomechanics of Plasticity and Fracture*. Cambridge University Press, 1992.
- [52] S. Nishimura. *Laboratory study on anisotropy of natural London Clay*. PhD thesis, Imperial College London, November 2005.
- [53] S. Nishimura, N. Minh, and R. Jardine. Shear strength anisotropy of natural London clay. *Géotechnique*, 57(1):49–62, 2007.
- [54] R. Parry. Correspondence on *On yielding of soils*. *Géotechnique*, 8:183–186, 1958.
- [55] J. Pestana and A. Whittle. Formulation of a unified constitutive model for clays and sands. *Int. J. Numer. Anal. Meth. Geomech.*, 23(12):1215–1243, 1999.
- [56] A. Puzrin and G. Houlsby. Fundamentals of kinematic hardening hyperplasticity. *International Journal of Solids and Structures*, 38(21):3771–3794, 2001.
- [57] A. Puzrin and E. Kirschenboim. Kinematic hardening model for overconsolidated clays. *Computers and Geotechnics*, 28(1):1–36, 2001.
- [58] K. Roscoe and J. Burland. On the generalised stress-strain behaviour of wet clay. In J. Hayman and F. Leckie, editors, *Engineering Plasticity*, pages 535–609. Cambridge Univeristy Press, 1968.
- [59] K. Roscoe, A. Schofield, and C. Wroth. On the yielding of soils. *Géotechnique*, 8(1):22–53, 1958.
- [60] A. Schofield and P. Wroth. *Critical State Soil Mechanics*. McGraw-Hill Publishing Company Limited, 1968.
- [61] J. Simo and R. Taylor. Consistent tangent operators for rate-independent elastoplasticity. *Comput. Methods Appl. Mech. Eng.*, 48(1):101–118, 1985.
- [62] N. Sivasithamparam, D. Kamrat-Pietrasewska, and M. Karstunen. An anisotropic bubble model

- for soft clays. In *7th European Conference on Numerical Methods in Geotechnical Engineering (NUMGE)*, pages 21–26, 2010.
- [63] F. Tavenas, J.-P. Des Rosiers, S. Leroueil, P. L. Rochelle, and M. Roy. The use of strain energy as a yield and creep criterion for lightly overconsolidated clays. *Géotechnique*, 29(3):285–303, 1979.
- [64] J. Tejchman and A. Niemunis. Fe-studies on shear localization in an anisotropic micro-polar hypoplastic granular material. *Granular Matter*, 8(3):205–220, 2006.
- [65] S. Wheeler, A. Näätänen, M. Karstunen, and M. Lojander. An anisotropic elastoplastic model for soft clays. *Canadian Geotechnical Journal*, 40(2):403–418, 2003.
- [66] A. Whittle and M. Kavvas. Formulation of MIT-E3 constitutive model for overconsolidated clays. *Journal of Geotechnical Engineering*, 120(1):173–198, 1994.
- [67] K. Willam and E. Warnke. Constitutive model for the triaxial behaviour of concrete. In *Proceedings of the May 17-19 1974, International Association of Bridge and Structural Engineers Seminar on Concrete Structures Subjected to Triaxial Stresses, held at Bergamo Italy*, 1974.
- [68] D. Wood. *Geotechnical Modelling*. Spon Press, Abingdon, 2004.
- [69] Y. Yamakawa, K. Hashiguchi, and K. Ikeda. Implicit stress-update algorithm for isotropic cam-clay model based on the subloading surface concept at finite strains. *International Journal of Plasticity*, 26(5):634–658, 2010.
- [70] C. Yang, J. P. Carter, and S. Yu. Comparison of model predictions of the anisotropic plasticity of lower cromer till. *Computers and Geotechnics*, 69:365 – 377, 2015.
- [71] C. Yang, D. Sheng, J. P. Carter, and S. W. Sloan. Modelling the plastic anisotropy of lower cromer till. *Computers and Geotechnics*, 69:22 – 37, 2015.
- [72] H. S. Yu. *Plasticity and Geotechnics*. Springer, 2006.
- [73] H. Ziegler. *An introduction to thermomechanics*. North Holland Pub. Co, Amsterdam, 2nd edn. edition, 1983.

## A Yield surface & flow rule

This section provides the derivation of the yield function and the direction of plastic flow from the dissipation function following the standard procedure as given by Coombs and Crouch [21]. First, we obtain the dissipative stresses through taking the partial derivatives of (5) with respect to the plastic strain rates, giving

$$p^\varphi = \frac{\partial \dot{\Phi}}{\partial \dot{\varepsilon}_v^p} = \frac{A^2(\dot{\varepsilon}^p + \beta_{ij}\dot{\gamma}_{ij}^p)}{\dot{\Phi}} \quad (29)$$

and

$$s_{ij}^\varphi = \frac{\partial \dot{\Phi}}{\partial \dot{\gamma}_{ij}^p} = \frac{B^2\dot{\gamma}_{ij}^p + A^2(\dot{\varepsilon}^p + \beta_{kl}\dot{\gamma}_{kl}^p)\beta_{ij}}{\dot{\Phi}}. \quad (30)$$

Rearranging (29) and (30), the plastic strain rates are

$$\dot{\varepsilon}_v^p = \frac{p^\varphi \dot{\Phi}}{A^2} - \beta_{ij}\dot{\gamma}_{ij}^p \quad \text{and} \quad \dot{\gamma}_{ij}^p = \frac{\dot{\Phi}}{B^2}(s_{ij}^\varphi - p^\varphi\beta_{ij}). \quad (31)$$

Substituting (31) into (5), to eliminate the plastic strain rates, and rearranging, we obtain the instantaneous anisotropic dissipative yield function as

$$f^\varphi = (p^\varphi)^2 B^2 + \left(s_{ij}^\varphi - p^\varphi\beta_{ij}\right)\left(s_{ij}^\varphi - p^\varphi\beta_{ij}\right)A^2 - A^2 B^2 = 0. \quad (32)$$

From (32) it should be apparent that introducing a cross-coupling in the rate of dissipation function results in the dissipative yield surface being sheared off the hydrostatic axis, where  $\beta_{ij}$  is a second order, traceless (deviatoric), tensor measure of this inclination. If  $\beta_{ij} = 0$  we recover an isotropic dissipative yield surface, with the ellipsoid’s major axis coincident with the hydrostatic axis.

When  $s_{ij}^\varphi = p^\varphi \beta_{ij}$ , the dissipative pressure is equal to  $p^\varphi = \pm A$ . Here the stress state is located at the compressive and tensile limits of the yield surface in dissipative stress space. From (31)<sub>2</sub>, at these limits, the plastic shear strain rate is zero, defining the normal consolidation line (NCL) in dissipative stress space. For the tensile apex of the anisotropic yield surface to be at the origin in true stress space, the shift stress components must be linked through

$$s_{ij}^X = p^X \beta_{ij}, \quad (33)$$

and the individual shift stress components are

$$p^X = \frac{\gamma p_c}{2} \quad \text{and} \quad s_{ij}^X = \frac{\gamma p_c}{2} \beta_{ij}. \quad (34)$$

Using the relation that the dissipative stress is the difference between the Cauchy stress and the shift stress (that is,  $\sigma_{ij}^\varphi = \sigma_{ij} - \sigma_{ij}^X$ ), we obtain the yield function as

$$f = (p - \gamma p_c/2)^2 B^2 + (s_{ij} - p \beta_{ij})(s_{ij} - p \beta_{ij}) A^2 - A^2 B^2 = 0. \quad (35)$$

Diving by  $p_c^4$ , rearranging and simplifying, the dimensionless anisotropic yield surface in true stress space becomes

$$f = \gamma(2 - \gamma)(\bar{p} - 1)\bar{B}^2 + r_{ij}^\beta r_{ij}^\beta \bar{p} \bar{A}^2 = 0, \quad (36)$$

where  $r_{ij}^\beta = r_{ij} - \beta_{ij}$ ,  $r_{ij} = s_{ij}/p$ ,  $\bar{p} = p/p_c$  and

$$\bar{A} = (1 - \gamma)\bar{p} + \frac{\gamma}{2} \quad \text{and} \quad \bar{B} = \bar{\rho}(\theta)M\left((1 - \alpha)\bar{p} + \frac{\alpha\gamma}{2}\right). \quad (37)$$

The direction of plastic flow in dissipative stress space is given by the derivative of (32) with respect to  $\sigma_{ij}^\varphi$

$$(f^\varphi, \varphi)_{ij} = \frac{2}{3} B^2 \left( p^\varphi + A^2 (p^\varphi \beta_{kl} - s_{kl}^\varphi) \beta_{kl} \right) \delta_{ij} + 2A^2 (s_{ij}^\varphi - p^\varphi \beta_{ij}). \quad (38)$$

Substituting for the dissipative stresses,  $\sigma_{ij}^\varphi = \sigma_{ij} - \sigma_{ij}^X$ , and normalising with respect to  $p_c^3$ , we obtain the direction of plastic flow in true stress space as

$$(g, \sigma)_{ij} = \frac{2}{3} \left( \bar{B}^2 (\bar{p} - \gamma/2) - \bar{A}^2 \bar{p} r_{kl}^\beta \beta_{kl} \right) \delta_{ij} + 2\bar{A}^2 \bar{p} r_{ij}^\beta. \quad (39)$$

## B Algorithmic implementation

The main part of the paper provides details on the algorithmic development of the anisotropic model. The model can be summarised using six key equations:

- (2) the elastic free energy function providing a relationship between the elastic strain and the Cauchy stress;
- (5) dissipation function, providing the yield function and direction of plastic flow;
- (12) an equation linking the current level of anisotropy to the shape parameter,  $\gamma$ ;
- (13) an equation linking the current level of anisotropy to the shape parameter,  $\alpha$ ;
- (18) an isotropic hardening law controlling the hydrostatic extent of the yield surface; and
- (19) an anisotropic hardening law controlling the shearing of the yield envelope.

However, these equations only provide a rate description of the model. In order for the model to be used in practical boundary value simulations (or even at a material point simulation level), these rate equations must be reformulated into an incremental relationship. Here a fully implicit backward Euler (bE) stress integration scheme is used. Note, that in this section we shift to matrix/vector notation to provide enhanced clarity for numerical implementation.

First, implicit integration of (18) and (19) yields the following evolution laws

$$\tilde{p}_c = \frac{p_{c_n}}{1 - (\Delta\varepsilon_v^p + \{\Delta\gamma^p\}^T\{\beta\})/(\lambda - \kappa)} \quad (40)$$

and

$$\{\tilde{\beta}_{n+1}\} = \frac{\{\beta_n\} + C_\beta x_\beta \|\{\Delta\gamma^p\}\| \{\bar{r}^\beta\}}{1 + C_\beta \|\{\Delta\gamma^p\}\|} \quad (41)$$

The subscript  $n$  denotes the previously converged solution associated with the last step (or the initial state at the start of the analysis). Here, we denote these evolution equations with a tilde to distinguish them from incremental updating through the bE method.

Using the following fourteen dimensionless residuals

$$\{b\} = \{\{\varepsilon^e\} - \{\varepsilon_t^e\} + \Delta\gamma\{g,\sigma\} \quad 1 - \tilde{p}_c/p_c \quad \{\beta\} - \{\tilde{\beta}\} \quad f\}^T \quad (42)$$

and taking the derivative of the residuals respect to the following set of unknowns

$\{x\} = \{\{\varepsilon^e\} \quad p_c \quad \{\beta\} \quad \Delta\gamma\}^T$ , the (14×14) Hessian matrix is obtained as

$$[A] = \left[ \frac{\partial b}{\partial x} \right] = \begin{bmatrix} [I] + \Delta\gamma[g,\sigma\sigma][D^e] & \Delta\gamma\{g,\sigma p_c\} & \Delta\gamma\{g,\sigma\beta\} & \{g,\sigma\} \\ -\{(\tilde{p}_c/p_c),\sigma\}^T [D^e] & -(\tilde{p}_c/p_c),p_c & -\{(\tilde{p}_c/p_c),\beta\}^T & -(\tilde{p}_c/p_c),\Delta\gamma \\ -[\tilde{\beta},\sigma][D^e] & -\{\tilde{\beta},p_c\} & [I] - [\tilde{\beta},\beta] & -\{\tilde{\beta},\Delta\gamma\} \\ \{f,\sigma\}^T [D^e] & f,p_c & \{f,\beta\}^T & 0 \end{bmatrix} \quad (43)$$

The iterative increment in the unknowns is given by

$$\{\delta x\} = -[A]^{-1}\{b\}. \quad (44)$$

The iterative increment of  $(\cdot)$  is denoted by  $\delta(\cdot)$  using a lower-case delta to denote that this increment is the contribution to the unknowns for a given iteration. The total increment in the unknowns,  $\{\Delta x\}$ , is given by the summation of the iterative increments over the number of iterations required to converge within a specified tolerance. The iterative procedure starts from the following initial conditions  $\{^0\varepsilon^e\} = \{\varepsilon_t^e\}$ ,  $^0\Delta\gamma = 0$ ,  $^0p_c = p_{c_t}$  and  $\{^0\beta\} = \{\beta_t\}$ , the pre-superscript denotes the iteration number and  $(\cdot)_t$  denotes a trial value. That is,  $f_t$  is the value of the yield function at the trial stress state and  $p_{c_t}$  and  $\{\beta_t\}$  are the trial values of the size of the yield surface and the level of anisotropic shearing. For small strain analysis, these trial values are equal to the value of the parameter determined at the previously converged state. The Newton-Raphson iterative process continues until the residuals converge to within a specified tolerance on each of the four grouped residuals, typically  $1 \times 10^{-9}$ . Throughout the stress return, all of the derivatives are evaluated at the current state. This requires the repeated evaluation of the derivatives at each iteration in addition to the inversion of the Hessian matrix (43) and ensures that the consistency condition is satisfied at the updated state (including all of the stress and internal variable dependent parameters, such as  $\alpha$  and  $\gamma$ ). For the sake of brevity, the lengthy derivatives are omitted.